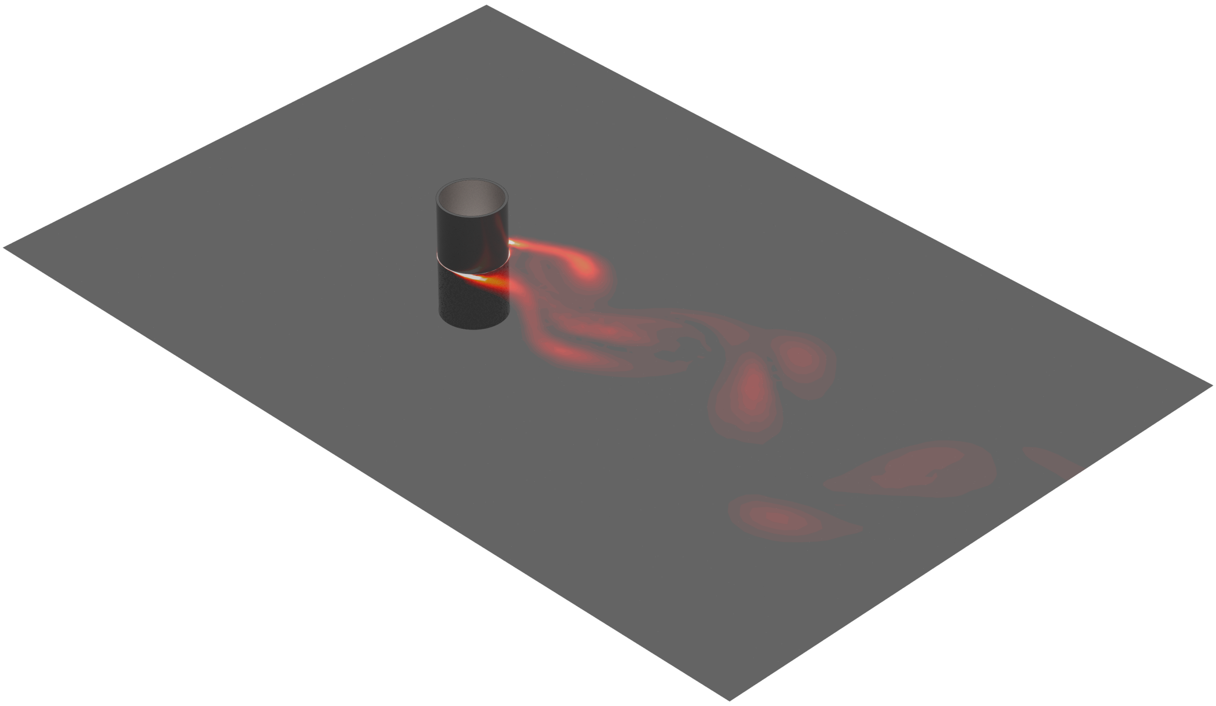

Assessment of segment-level vortex-induced vibration response of a deepwater drilling riser using high-fidelity modelling

Master's thesis in Marine Technology, Mobility Engineering Programme

VIJAY PAL-SINGH

DEPARTMENT OF MECHANICS AND MARITIME SCIENCES
CHALMERS UNIVERSITY OF TECHNOLOGY
Gothenburg, Sweden 2026
www.chalmers.se

Master's thesis in mobility engineering

Assessment of segment-level vortex-induced vibration response of a deepwater drilling riser using high-fidelity modelling

VIJAY L. PAL-SINGH

CHALMERS
UNIVERSITY OF TECHNOLOGY

Department of Mechanics and Maritime Sciences
Division of Marine Technology
Chalmers University of Technology
Göteborg, Sweden 2026

Assessment of segment-level vortex-induced vibration response
of a deepwater drilling riser using high-fidelity modelling
VIJAY L. PAL-SINGH

Supervisor 1: Mohd Atif Siddiqi, Kongsberg Maritime, Advanced Marine Operations
Supervisor 2: Bernt Johan Leira, Department of Marine Technology, NTNU
Examiner: Jonas Ringsberg, Department of Mechanics and Maritime Sciences

Department of Mechanics and Maritime Sciences
Division of Marine Technology
Chalmers University of Technology
SE-412 96 Göteborg, Sweden
Telephone: +46 (0)31 772 1000

Cover: Kármán vortex street CFD visualization behind riser segment

Typeset in LaTeX
Printed by Chalmers Reproservice
Göteborg, Sweden 2026

Assessment of segment-level vortex-induced vibration response of a deepwater drilling riser using high-fidelity modelling

Master's thesis in Mobility Engineering
VIJAY L. PAL-SINGH
Department of Mechanics and Maritime Sciences
Division of Marine Technology
Chalmers University of Technology

Abstract

Based on the literature reviewed, few studies have analysed the vortex-induced vibration response of a low-aspect-ratio computational fluid dynamics riser model, and the use of dynamic properties derived from a global riser model appears to be largely unexplored. A realistic deepwater drilling riser with buoyancy modules is modelled in OrcaFlex, an extensively-used offshore industry software, using a wake oscillator model. Separately, a short segment of this riser is modelled in CFD using Star-CCM+ in a two-way fluid-structure interaction setup. The segment's physical, environmental, and dynamic properties are derived from a selected segment in the full-scale riser model in OrcaFlex. The dynamic current-induced VIV response of the segment is compared between OrcaFlex and Star-CCM+ to determine whether the responses are comparable. It is seen that both models display similar dominant response, dominant lift frequencies, and lock-in behaviour across a range of current velocity cases. The RMS cross-flow displacement and lift coefficient present a similar trend across cases, except in cases with significant changes in top tension, in which the RMS values diverge significantly between the full-scale riser model in OrcaFlex and the riser segment model in Star-CCM+. These results indicate that high-fidelity modelling of short riser segments can reproduce the VIV response metrics of a global wake oscillator riser model under various conditions, except in cases where the top tension is changed significantly and complicates global riser dynamics.

Keywords: computational fluid dynamics, drilling riser, fluid-structure interaction, lock-in, riser segment, vortex-induced vibrations

Preface and Acknowledgements

The thesis work is representative of two years of maritime engineering education in Norway and Sweden as part of the Nordic Five Tech university collaboration initiative. The work was done in partnership with the Advanced Marine Operations division of Kongsberg Maritime.

I would like to express my sincere appreciation to the following individuals:

To my main supervisor and examiner, Jonas Ringsberg, for your guidance in helping me understand the technical framework of the thesis. Your advice was crucial for the initiation and the development of the thesis.

To my co-supervisor, Bernt Johan Leira, for your dedicated expertise in the field of marine structures, which provided a thorough, technical backbone to my work.

To my industry co-supervisor, Mohd Atif Siddiqui, for your instrumental knowledge in offshore drilling risers. Our discussions gave me an appreciation for the complex nature of structural modelling in the offshore environment.

Vijay L. Pal-Singh, Gothenburg, May 2026

Contents

List of Figures

List of Tables

List of Abbreviations

Abbreviation	**–**	**Description**
BOP	–	Blowout preventer
CFD	–	Computational fluid dynamics
DOF	–	Degree of freedom
FFT	–	Fast Fourier transform
FSI	–	Fluid-structure interaction
LMRP	–	Lower marine riser package
RMS	–	Root mean square
SST	–	Shear stress transport
URANS	–	Unsteady Reynolds-averaged Navier–Stokes
VIV	–	Vortex-induced vibration

List of Variables

Variable	**[Unit]**	**Description**
A	[m]	Displacement amplitude
A_i	$[m^2]$	Internal cross-sectional area of riser
a_0	[-]	Linear damping coefficient
a_1	[-]	Linear restoring coefficient
a_2	[-]	Non-linear stiffness coefficient
a_3	[-]	Non-linear damping coefficient
a_4	[-]	Coupling coefficient
B_n	[N]	Net buoyancy uplift
c	$[N \cdot s/m]$	Damping coefficient
c_x	$[N \cdot s/m]$	Inline damping coefficient
c_y	$[N \cdot s/m]$	Cross-flow damping coefficient
C_h	[-]	Hydrodynamic damping matrix
D	[m]	Cylinder or riser diameter
D_b	[m]	Buoyant section outer diameter
D_i	[m]	Riser inner diameter
D_o	[m]	Riser outer diameter
d_m	$[kg/m^3]$	Drilling fluid density
d_w	$[kg/m^3]$	Seawater density
F	[N]	Applied support force vector
F_D	[N]	Hydrodynamic drag force
F_L	[N]	Hydrodynamic lift force
f_n	[Hz]	Natural frequency
f_s	[Hz]	Vortex shedding frequency
f_{bt}	[-]	Buoyancy tolerance factor
f_{wt}	[-]	Weight tolerance factor
g	$[m/s^2]$	Gravitational acceleration
H_m	[m]	Drilling fluid column height
H_w	[m]	Seawater column height
k	[N/m]	Stiffness coefficient
k_x	[N/m]	Inline stiffness coefficient
k_y	[N/m]	Cross-flow stiffness coefficient
K_h	[-]	Hydrodynamic stiffness matrix
L_b	[m]	Length of buoyant section
L_r	[m]	Total riser length
m	[kg/m]	Mass per unit length
m^*	[-]	Mass ratio
m'_{steel}	[kg/m]	Dry mass of steel riser per unit length

Variable	[Unit]	Description
m'_{buoy}	[kg/m]	Dry mass of buoyancy material per unit length
m_x	[kg]	Inline mass
m_y	[kg]	Cross-flow mass
n	[-]	Number of failed tensioners
N	[-]	Total number of tensioners
q	[-]	Wake oscillator variable
q_0	[-]	Initial wake oscillator value
R_f	[-]	Reduction factor for tension calculation
St	[-]	Strouhal number
T	[N]	Effective tension
T_{MIN}	[N]	Minimum required top tension
T_{SRmin}	[N]	Minimum slip ring tension
U	[m/s]	Current velocity
U_r	[-]	Reduced velocity
u_x	[m]	Inline displacement
u_y	[m]	Cross-flow displacement
v_x	[m/s]	Inline velocity
v_y	[m/s]	Cross-flow velocity
x	[m]	Inline displacement
$\dot{x}$	$[m/s]$	Inline velocity
$\ddot{x}$	$[m/s^2]$	Inline acceleration
y	[m]	Cross-flow displacement
$\dot{y}$	$[m/s]$	Cross-flow velocity
$\ddot{y}$	$[m/s^2]$	Cross-flow acceleration
z	[m]	Axial coordinate
ϵ	[-]	Non-linear damping parameter
ζ	[-]	Damping ratio
ν	$[m^2/s]$	Kinematic viscosity
ω_s	[rad/s]	Shedding frequency
ρ	$[kg/m^3]$	Fluid density
ρ_w	$[kg/m^3]$	Seawater density

1

Introduction

The purpose of this chapter is to describe the relevance of this study in the context of offshore drilling. The core objectives and structure of the study are presented, as well as the bounds which characterise the study's scope.

1.1 Background

1.1.1 The top-tensioned drilling riser

An offshore riser is a conduit used in the oil and gas industry to carry operating fluids between the wellhead and the floating vessel or platform. Production risers carry crude oil, while drilling risers carry drilling fluids to remove drilling debris from the bore hole and provide a pathway to lower drilling tools into the well.

Drilling risers are equipped with a tensioner system, shown in Figure 1.1, composed of tensioner cylinders which can be hydropneumatic, hydraulic, or mechanical in nature, which keeps the riser under nearly constant axial force by acting as a controlled spring-damper mechanism. Such a system prevents riser motion due to vessel heave, and acts primarily as a means to balance riser weight and to prevent compression and buckling. Through applied tension, it also influences the riser's geometric stiffness, which can shift the riser's natural frequencies.

As shown in Figure 1.2, the tensioner cylinders are attached to the tensioner ring which, integrated with the outer barrel of the telescoping joint, transfers the axial loads from the riser and the applied tension from the tensioners.

The wellhead, located above the bore hole, is fitted with a blowout preventer (BOP), which prevents uncontrolled flow from the well system, and lower marine riser package (LMRP), which allows the drilling rig to disconnect quickly and safely from the BOP during an emergency.

The upper flex joint and lower flex joint provide controlled rotation to the top and bottom ends of the riser. Though the surface vessel typically has a dynamic positioning system to remain within close range of its initial position, the riser nevertheless experiences bending loads which, if not transferred effectively, can damage the riser at the top end and damage the BOP and LMRP at the bottom end.

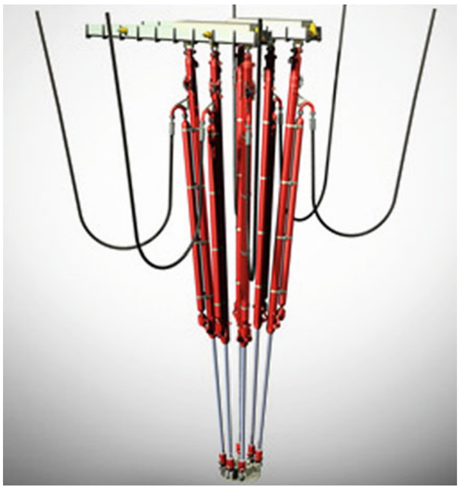

Figure 1.1: Drilling rig tensioner system

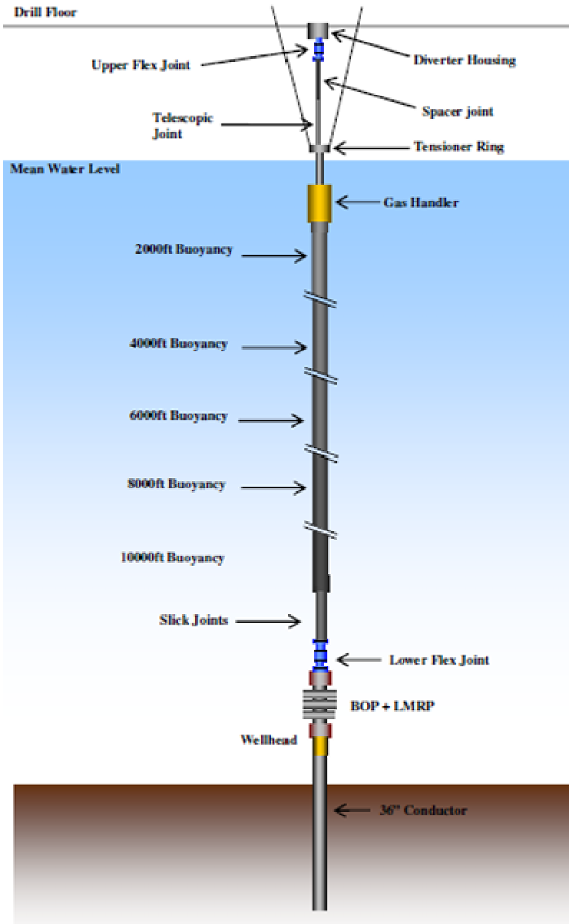

Figure 1.2: Drilling riser design

Buoyancy modules, composed of low density syntactic foam, are installed along a section of the riser to reduce the amount of top tension required to support the weight of the riser, riser components and the riser's internal contents, usually drilling fluid. Figure 1.3 shows the arrangement of a drilling riser joint with buoyancy modules encasing the riser and auxiliary lines.

Figure 1.3: Riser joint with buoyancy module

In addition to buoyancy modules, VIV suppression devices such as fairings and helical strakes, shown in Figure 1.4, are usually installed along the riser to disrupt and minimise vortex formation.

(a) Fairing (b) Helical strake

Figure 1.4: VIV suppression devices

The vortex formation, also called vortex shedding, along a top-tensioned drilling riser induces a structural response called vortex-induced vibration, and it can become especially problematic when the vortex shedding frequency synchronises with the riser's natural frequency in a resonant phenomenon called lock-in, further described in detail in chapter 2.

1.1.2 Vortex-induced vibrations in drilling risers

In the deepwater environment, the susceptibility to vortex-induced vibrations arises from the riser's long, slender geometry, which causes it to behave as a flexible cylinder. Though the top tensioners and buoyancy modules act together to increase the riser's geometric stiffness, the riser is nevertheless subject to the effects of its complex environmental conditions, which include forces due to waves, wind, and current. Ocean currents vary in magnitude depending on the location of the drilling operation, but they typically have a sheared profile due to the differences in water density in relation to depth. Surface currents are driven by global wind systems, while deep ocean currents arise from global differences in water density (NOAA, 2025).

Drilling risers are continuously monitored for structural integrity by using simulation software to assess the structural dynamics of the riser in response to environmental loads. Drilling operators can therefore be better informed about the safety of the equipment with regards to the local environmental conditions of the drilling operation. Among the various tools that may be used to assess riser structural dynamics, OrcaFlex, developed by Orcina, is regarded as an industry standard tool because it can capture the dynamics of a large, complex system with sufficient accuracy and within a relatively short simulation time compared to CFD tools which are too expensive computationally for the large nature of the drilling riser.

OrcaFlex version 11.6b is used in this study. To simulate vortex-induced vibrations, OrcaFlex offers wake oscillator models and vortex tracking models, which are both reduced order models developed from empirical data and experiments, and the simulation results can be exported to software such as Shear7 and VIVANA for specialised VIV fatigue assessments. OrcaFlex's wide array of robust features is also a reason it is used frequently for global VIV analysis. In local, critical sections, however, such as connector regions, buoyancy module transition regions, or regions with installed VIV suppression devices, OrcaFlex may not be the most suitable tool because it cannot capture the underlying fluid flow interaction with the structure's surface. In such a case, a higher fidelity modelling approach using a computational fluid dynamics tool such as Star-CCM+ may be warranted to capture the detailed fluid-structure interaction of vortex shedding.

The modelling of vortex-induced vibrations using a CFD tool is not by any means a novel idea. For instance, in a research project conducted by Chen et al. (2006), two-dimensional and three-dimensional simulations of flow past an elastically supported riser of low aspect ratio were performed and compared to assess the accuracy of CFD modelling of VIV in high Reynold's number flows. The low aspect ratio refers to the riser's length to diameter ratio, though the aspect ratio used in this research initiative was 1400, which is still considerably high. The VIV response of cylinders of lower aspect ratios has been studied, as well, for low Reynold's number flows (Cajas et al., 2023), but to a limited degree and not within the high Reynold's number regime of offshore current flow.

The novelty of this thesis lies not in the CFD modelling of a riser which has been thoroughly researched, nor does it lie in the CFD modelling of a low aspect ratio cylinder. However, the development of an independent CFD model of a short riser segment with derived environmental, physical, and dynamic properties from a global riser model to analyse the CFD model's response to VIV has not been attempted in the past. This study evaluates the suitability of CFD modelling of a low aspect ratio cylinder with dynamic similarity to a global riser model for VIV prediction. A model of this nature is particularly relevant due to the high computational cost of a CFD riser model of high aspect ratio.

Star-CCM+ is a multi-physics, computational fluid dynamics software from Siemens used in many engineering fields to simulate fluid flow scenarios, and it is the CFD tool of choice to model the riser segment in this study due to its advanced features and its ability to model two-way FSI within the same computational environment. Star-CCM+ version 2506.0001 is used in this study.

1.2 Objectives

The general objective of this thesis is to investigate the vortex-induced vibrational response of both a high-fidelity CFD model of a short riser segment and a low-fidelity, global drilling riser model.

To achieve this aim, the specific research objectives were defined as follows:

1. Develop a realistic, low-fidelity drilling riser model in OrcaFlex using a wake oscillator to simulate VIV.

2. Select a VIV-sensitive segment of the riser in OrcaFlex and develop a high-fidelity CFD model of the segment in Star-CCM+ using a two-way FSI interface.

3. Run both models under the same conditions and compare the predicted VIV amplitudes and dominant frequencies.

4. Investigate the influence of velocity profile and magnitude and the variation of riser top tension on the VIV predictions of both models.

5. Evaluate the ability of the high-fidelity CFD model to capture the local riser dynamic VIV response predicted by the low-fidelity drilling riser model.

6. Identify the strengths and limitations of the high-fidelity model and the low-fidelity model.

1.3 Thesis structure

The thesis begins with an introduction to the project with the chosen scope and limitations aligned with the thesis objectives. Chapter 2 presents a literature review and the theory required to understand the underlying physics of vortex shedding, followed by an in-depth characterisation of the global riser model defined in OrcaFlex and the fluid-structure interaction model defined in STAR-CCM+. Chapter 3 describes the methodology employed in building the two models, including modelling choices and simulation parameters. In chapter 4, the results are extracted from both model simulations with a sensitivity analysis to assess model behaviour in response to current inflow conditions. Chapter 5 proceeds with a discussion of results and their significance with respect to riser design and analysis. In chapter 6, conclusions of the thesis work are presented with key findings and how they answer the research objective stated in section 1.2. Finally, in chapter 7, recommendations for future work are proposed with a discussion of possible modelling improvements and methods to increase the reliability of high-fidelity simulation of short riser segments.

1.4 Scope and limitations

This thesis examines to what extent a short segment model derived from a full-scale deepwater riser model can reproduce an equivalent vortex-induced vibrational response in a two-way fluid-structure interaction configuration using computational fluid dynamics. The study presents certain limitations which must be addressed to clarify the scope.

First, the deepwater riser model in OrcaFlex ignores the effect of torsion, as well as the effects of wind and wave forces, and only includes current forces in the environment. Second, the Iwan and Blevins wake oscillator model is used in OrcaFlex to generate the vortex-induced vibrational response of the structure using the model default coefficients, which Orcina advises to remain unchanged. The wake oscillator coefficients have been developed using empirical and experimental data, but may in this regard limit or dampen the riser's response to VIV in certain conditions. The general findings are applicable to the simplified drilling riser configuration in OrcaFlex, including the use of default coefficients in the Iwan and Blevins wake oscillator model, and should not be generalised to full-scale, offshore drilling riser conditions until the model has been validated using field data.

The high-fidelity model in Star-CCM+ derives its properties, boundary conditions, and local environmental conditions from the drilling riser model in OrcaFlex; therefore, the results of this study are dependent on the simplified riser physical configuration in OrcaFlex. Furthermore, the CFD model is limited to 2-DOF motion which applies to the lateral x and y planes, and it is constrained in the axial direction. The axial stiffness is magnitudes of order higher than the lateral stiffnesses, which may reduce the impact of this limitation. Another important limitation of the CFD model is its low aspect ratio, which makes the VIV behaviour sensitive to free end effects. The model's lock-in behaviour is still tied to the structural vibration dynamic properties derived from the global riser model, but the free end effects still alter the wake mechanism behind the cylinder. The general findings in this model are applicable to the simplified 2-DOF riser model of a low aspect ratio and should not be generalised to high aspect ratio riser models or riser models with higher degrees of freedom.

2

Literature review and theory

This chapter achieves two purposes. The first is to present how this study fits into and contributes to past research of vortex-induced vibrations. The second is to provide the important theory and principles of VIV, which are necessary to understand the underlying physics that the study aims to represent in the simulation models.

2.1 Literature review

As mentioned previously in subsection 1.1.2, the physics of vortex-induced vibrations has been the subject of extensive research in past decades. Griffin et al. (1973) performed a series of experiments to examine the vortex-excited oscillations of circular cylinders in cross flow, followed by Sarpkaya (1977) who sought to estimate experimentally the in-line and transverse forces of cylinders in oscillatory flow. Nearly three decades later, Jauvtis and Williamson (2003) studied the VIV response of an elastically mounted cylinder, free to move in two degrees of freedom, in an experimental water channel facility. The 2-DOF XY cylinder motion has been of particular interest lately. As noted by Williamson and Jauvtis (2004) in a separate study, for bodies of mass ratio $m* > 6$, the in-line oscillations have a negligible effect on the cross-flow oscillations, and in many cases the Y-only motion may be sufficient for the study of VIV; however, for bodies of mass ratio $m* < 6$, the oscillations in the in-line direction begin to have an important effect on the cross-flow behaviour. The mass ratio is expressed as $m^* = \frac{m}{\frac{\pi}{4}\rho D^2}$, where m is the mass of the cylinder and the denominator is the mass of displaced fluid. In hydrodynamic applications such as in this study, the mass ratio is typically quite low, often below 10, which necessitates the study of VIV in two degrees of freedom.

More recently, in the context of offshore riser modelling, Chen et al. (2006) conducted research on using computational fluid dynamics to simulate three-dimensional flow past an elastically supported riser of low aspect ratio at high Reynold's numbers, which is more consistent with offshore fluid dynamics. Due to the high computational cost of CFD simulations, cylinders of lower aspect ratio have been the subject of further research to decrease the aspect ratio while minimising the cylinder end effects on VIV behaviour. Cajas et al. (2023) studied the influence of cylinder aspect ratio on VIV behaviour at low Reynold's numbers, testing aspect ratios of 2, 3, 5, and 7, and concluded that the free ends have an important influence on the VIV behaviour of a cylinder of low aspect ratio. Zhao and Cheng (2014) conducted a similar study and concluded that for a finite cylinder with an aspect ratio of 1 and 2, the free end effects strongly affect the cylinder's wake structure and can even alter lock-in behaviour. However, the paper also states that, though the wake mechanism changes due to the free end effects, the peak vibration frequency remains close to the structural natural frequency. This is an important limitation that must be understood regarding simulations of finite cylinders of low aspect ratio: though the free end effects alter the vortex formation behind the cylinder, the lock-in behaviour remains closely tied to the structure's vibration dynamics.

2.2 Theory

2.2.1 Vortex shedding

Vortex shedding occurs when flow separation across a bluff body causes alternating vortices to form downstream of the body in a pattern known as a von Kármán vortex street (Huang et al., 2022). Flow separation depends on both the fluid velocity and the fluid's kinematic viscosity; therefore, vortex shedding cases are categorised using the Reynold's number, expressed as $Re = \frac{UD}{\nu}$, where U is the flow velocity in m/s, D is the outer diameter of the cylindrical body in m, and ν is the kinematic viscosity in m^2/s. Vortex shedding across an oscillatory cylinder can be expressed in the Strouhal relation as $St = \frac{f_s D}{U}$ where St is the Strouhal number which takes a value of 0.2 for 300 < Re < 300 000, considered the subcritical flow regime.

2.2.2 Drag and lift

Due to the unsteady pressure distributions around the cylinder, vortex shedding generates both lift and drag forces, which are defined as fluctuating and expressed in Equation 2.1 and Equation 2.2 (Modarres-Sadeghi, 2022).

$$F_L(t) = \frac{1}{2}\rho D U^2 C_L' \sin(\omega_s t + \alpha) \tag{2.1}$$

$$F_D(t) = \frac{1}{2}\rho D U^2 C_D' \sin(2\omega_s t + \beta) \tag{2.2}$$

where $\omega_s = 2\pi f_s$, C_L and C_D are the lift and drag coefficients, and α and β represent the phase of the signal.

The terms α and β are usually not equal because there exists a lag between the lift acting on the cylinder and the cylinder's response. In addition, the drag's frequency is defined as twice the shedding frequency only for certain cases, for instance during cylinder resonance. In other cases, the drag frequency may be defined differently.

2.2.3 Mass-spring-damper system vibration

The equation of motion for a forced vibration, damped 1-DOF Mass-spring-damper system is expressed in Equation 2.3.

$$m\ddot{y} + c\dot{y} + ky = F(t) \tag{2.3}$$

where F(t) is the excitation force expressed in N.

In matrix form:

$$\begin{bmatrix} m \end{bmatrix} \begin{Bmatrix} \ddot{y} \end{Bmatrix} + \begin{bmatrix} c \end{bmatrix} \begin{Bmatrix} \dot{y} \end{Bmatrix} + \begin{bmatrix} k \end{bmatrix} \begin{Bmatrix} y \end{Bmatrix} = \begin{Bmatrix} F_y(t) \end{Bmatrix} \tag{2.4}$$

In a 2-DOF uncoupled system, the motion takes the following matrix form:

$$\begin{bmatrix} m_x & 0 \\ 0 & m_y \end{bmatrix} \begin{Bmatrix} \ddot{x} \\ \ddot{y} \end{Bmatrix} + \begin{bmatrix} c_x & 0 \\ 0 & c_y \end{bmatrix} \begin{Bmatrix} \dot{x} \\ \dot{y} \end{Bmatrix} + \begin{bmatrix} k_x & 0 \\ 0 & k_y \end{bmatrix} \begin{Bmatrix} x \\ y \end{Bmatrix} = \begin{Bmatrix} F_x(t) \\ F_y(t) \end{Bmatrix} \tag{2.5}$$

In a 2-DOF fully coupled system, the off-diagonals are non-zero, at which point the stiffness matrix takes on the form expressed in Equation 2.6, and the damping matrix takes on the form expressed in Equation 2.7.

$$\mathbf{K} = \begin{bmatrix} k_{xx} & k_{xy} \\ k_{yx} & k_{yy} \end{bmatrix} \tag{2.6}$$

$$\mathbf{C} = \begin{bmatrix} c_{xx} & c_{xy} \\ c_{yx} & c_{yy} \end{bmatrix} \tag{2.7}$$

In fluid-structure interaction, the system is fully coupled through the hydrodynamic forces; however, the structural supports at either end may be uncoupled. Such a system would be defined by the matrix form in Equation 2.8.

$$\begin{bmatrix} m_x & 0 \\ 0 & m_y \end{bmatrix} \begin{Bmatrix} \ddot{x} \\ \ddot{y} \end{Bmatrix} + \begin{bmatrix} c_x & 0 \\ 0 & c_y \end{bmatrix} \begin{Bmatrix} \dot{x} \\ \dot{y} \end{Bmatrix} + \begin{bmatrix} k_x & 0 \\ 0 & k_y \end{bmatrix} \begin{Bmatrix} x \\ y \end{Bmatrix} = \begin{Bmatrix} F_D(x, y, \dot{x}, \dot{y}, t) \\ F_L(x, y, \dot{x}, \dot{y}, t) \end{Bmatrix} \tag{2.8}$$

In this matrix form, the lift and drag forces that define the excitation forces both depend on motion in x and y, which make them coupled; however, the left-hand side is decoupled. This represents the structural equation of motion.

In the overall fluid-structure interaction system, there is hydrodynamic coupling. To represent the overall system behaviour, not just the structural representation, the matrix form is written as the following:

$$\begin{bmatrix} m_x & 0 \\ 0 & m_y \end{bmatrix} \begin{Bmatrix} \ddot{x} \\ \ddot{y} \end{Bmatrix} + \left(\begin{bmatrix} c_x & 0 \\ 0 & c_y \end{bmatrix} + C_h \right) \begin{Bmatrix} \dot{x} \\ \dot{y} \end{Bmatrix} + \left(\begin{bmatrix} k_x & 0 \\ 0 & k_y \end{bmatrix} + K_h \right) \begin{Bmatrix} x \\ y \end{Bmatrix} = \begin{Bmatrix} F_D(t) \\ F_L(t) \end{Bmatrix} \tag{2.9}$$

where C_h is the hydrodynamic damping matrix and K_h is the hydrodynamic stiffness matrix.

2.2.4 Fluid-structure interaction

Fluid-structure interaction can be defined as either one-way or two-way. In one-way FSI, the fluid forces act on the structure, and the fluid loads induce structural deformation, but the structure's motion does not affect or significantly alter the fluid flow. The FSI interface is a one-way exchange of information from the fluid to the structure, and can be used reliably in applications where the structural motion is small and the FSI coupling is weak. On the other hand, two-way FSI is necessary in applications such as VIV modelling, in which the FSI coupling is strong and affects whether or not the structure enters resonance.

The dynamics of vortex-induced vibrations and the onset of frequency lock-in are affected and enabled by the two-way fluid-structure interaction coupling, shown in Figure 2.1, between the solid body and the surrounding fluid.

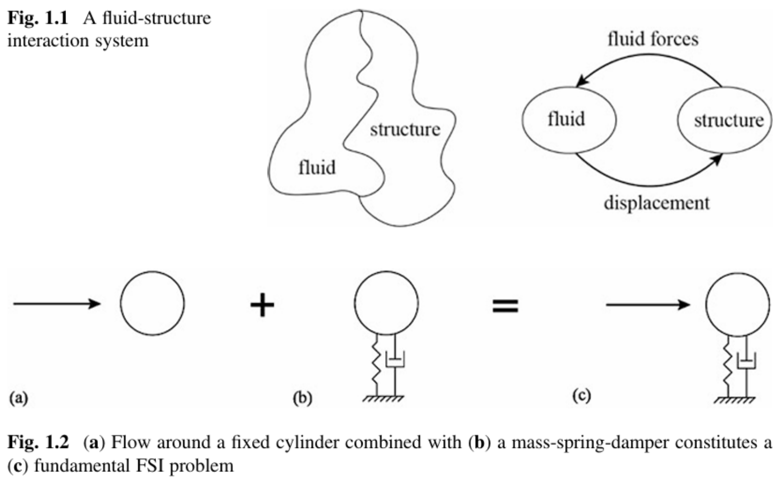

Figure 2.1: Fluid-structure interaction simplified diagram

In Star-CCM+, this interface allows for the exchange of data between the solid displacement and the mapped FSI traction, where the latter represents the transfer of fluid loads from the computational fluid dynamics solver to the structural solver. In two-way FSI, the coupling typically involves the following steps for each time step:

1. Wall pressure and shear forces computed from fluid loads

2. Mapped FSI traction

3. Solid deformation
4. Solid displacement mapped back to fluid mesh
5. Fluid mesh morphing
6. Repeat iterations until solution converges

Solution convergence refers to a state in the simulation in which successive solver iterations in both the fluid and solid domains satisfy the governing equations with negligible changes. When the interface displacement, force, and residuals, satisfy the convergence criteria, the simulation advances to the next time step.

2.2.5 Vortex-induced vibrations

The vortex-induced vibrations of a circular cylinder represent the cylinder's dynamic response to the fluctuating lift and drag forces due to vortex shedding. The fluid-structure interaction between the cylinder and the wake enables the lock-in phenomenon, in which the vortex shedding frequency aligns itself with the cylinder's nearest natural frequency. In such a case, the vortex shedding does not follow the Strouhal relation, and instead remains equal or close to the cylinder's natural frequency; lock-in is also characterised by large amplitudes of cylinder motion.

The lock-in range depends on two dimensionless parameters: the reduced velocity parameter expressed as $V_r = \frac{U}{f_n D}$, where f_n is the cylinder's natural frequency, and the mass ratio expressed as $m^* = \frac{m}{\frac{\pi}{4}\rho D^2}$, where m is the mass of the cylinder and the denominator is the mass of displaced fluid.

2.3 Vortex-induced vibration prediction models

The modelling of vortex-induced vibrations has been a topic of great interest. Apart from computational fluid dynamics (CFD) model which will be discussed in section 2.5, phenomenological models have been developed based on the van Der Pol equation expressed as:

$$\ddot{q} + \epsilon \left(q^2 - 1\right) \dot{q} + \omega_s^2 q = A\ddot{y} \tag{2.10}$$

where q is the wake oscillator variable and A and ϵ are constants derived from experimental data, and $\ddot{y}$ is the structural acceleration. The non-linear damping term $\epsilon\left(q^2 - 1\right)\dot{q}$ enforces the limit cycle behaviour of the wake, which represents the self-limiting aspect of the system.

The wake oscillator represents the wake being a cylinder using a single degree of freedom, represented by q in Equation 2.10. When the wake oscillates, it generates a lift force inducing cylinder motion; in response, the cylinder's acceleration feeds back into the wake, which creates a coupled non-linear system. The wake oscillator also only models the force in the transverse direction. The drag force is considered separately using the Morison's equation expressed as:

$$f = \underbrace{C_m \Delta a_f}_{\text{inertia}} + \underbrace{\frac{1}{2}\rho C_d A \left| v_f \right| v_f}_{\text{drag}} \tag{2.11}$$

f : fluid force (per unit length) on the body
C_m : inertia coefficient for the body
Δ : mass of fluid displaced by the body
a_f : fluid acceleration relative to earth
ρ : density of water
C_d : drag coefficient for the body
A : drag area
v_f : fluid velocity relative to earth

2.4 The OrcaFlex wake oscillator models

The wake oscillator models available in OrcaFlex include the Milan model and the Iwan and Blevins model. The Iwan and Blevins model is a classical wake oscillator model used to model vortex shedding and frequency lock-in. The model was calibrated using test data from fixed and forced cylinders, then compared to results from spring-mounted cylinders (Orcina, 2025). Unlike the Milan model, the Iwan and Blevins model transverse force accounts for the Morison drag force in the transverse direction; conversely, the Milan model does not include the drag force in the transverse direction. The two models are developed using different sets of empirical and experimental data, and the choice of the model depends on the application.

To understand the wake oscillator model in OrcaFlex, it is important to first understand that the riser model is a line type, which means that it is discretised into a finite element, lumped mass model, described by Orcina as "a series of lumps of mass joined together by massless springs" (Orcina, 2025). The lumps are denoted as nodes, and the springs are denoted as segments. The segments define the line's axial, bending, and torsional stiffnesses via spring-damper elements, whereas the nodes define the mass, weight, buoyancy, and drag properties of the line. When the Iwan and Blevins model is implemented, a flow velocity is required, provided by current, waves, or both. The wake oscillator is then applied to each segment along the riser. The spatial resolution of VIV depends on the level of segmentation, and a sensitivity analysis must be performed to ensure the model captures the VIV behaviour sufficiently in relation to the number of segments along the line. For each segment, OrcaFlex applies the wake oscillator, then calculates the generated lift force over the segment length.

2.5 High-fidelity CFD modelling for VIV prediction

2.5.1 The fluid volume

Star-CCM+, as many other computational fluid dynamics software, operates based on the fundamental laws of conservation of mass and conservation of momentum in the realm of continuum mechanics (Siemens, 2026), which can be described using the Navier-Stokes equation for incompressible fluids, written as:

$$\rho \left(\frac{\partial \mathbf{v}}{\partial t} + \mathbf{v} \cdot \nabla \mathbf{v} \right) = -\nabla p + \mu \nabla^2 \mathbf{v} + \mathbf{f} \tag{2.12}$$

where:

- ρ is the fluid density.
- $\mathbf{v}$ is the velocity vector.
- t is time.
- p is the pressure.
- μ is the dynamic viscosity.
- $\nabla^2 \mathbf{v}$ is the viscous diffusion term.
- $\mathbf{f}$ represents body forces acting on the fluid.

The equation is integrated over a discretised fluid volume using the finite volume method, a numerical method which uses the general transport equation shown in Equation 2.13 over a control volume V. This equation also uses the conservation of energy law, which is important in heat transfer problems.

$$\underbrace{\frac{d}{dt} \int_V \rho \phi \, dV}_{\text{Transient Term}} + \underbrace{\int_A \rho \mathbf{v} \phi \cdot d\mathbf{a}}_{\text{Convective Flux}} = \underbrace{\int_A \Gamma \nabla \phi \, d\mathbf{a}}_{\text{Diffusive Flux}} + \underbrace{\int_V S_\phi \, dV}_{\text{Source Term}} \tag{2.13}$$

where each term depends on the rate of change of the fluid property ϕ.

To model turbulence in the fluid volume, the Reynold's Averaged Navier-Stokes (RANS) model is used, in which the Navier-Stokes solution variable ϕ is decomposed into its mean variable and fluctuating component. The mean mass and momentum equations can then be written as in Equation 2.14 and in Equation 2.15.

$$\frac{\partial \rho}{\partial t} + \nabla \cdot (\rho \bar{\mathbf{v}}) = 0 \tag{2.14}$$

$$\frac{\partial}{\partial t}(\rho\bar{\mathbf{v}}) + \nabla\cdot(\rho\bar{\mathbf{v}}\otimes\bar{\mathbf{v}}) = -\nabla\cdot\bar{p}_{\mathrm{mod}}\mathbf{I} + \nabla\cdot\left(\bar{\mathbf{T}} + \mathbf{T}_{\mathrm{RANS}}\right) + \mathbf{f}_b \tag{2.15}$$

where:

- ρ is the density.
- $\bar{\mathbf{v}}$ is the mean velocity.
- $\bar{p}_{\mathrm{mod}} = \bar{p} + \frac{2}{3}\rho k$ is the modified mean pressure, where $\bar{p}$ is the mean pressure and k is the turbulent kinetic energy.
- $\mathbf{I}$ is the identity tensor.
- $\bar{\mathbf{T}}$ is the mean viscous stress tensor.
- $\mathbf{f}_b$ is the resultant of the body forces (such as gravity and centrifugal forces).
- $\bar{E}$ is the mean total energy per unit mass.
- $\bar{\mathbf{q}}$ is the mean heat flux.

T_{RANS} is a stress tensor quantity, defined by its magnitude and multi-plane directionality, that depends on the mean flow quantities of an eddy viscosity model. The eddy viscosity represents the additional momentum transport from turbulent eddies.

Star-CCM+ uses various eddy viscosity models, of which are the K-Epsilon ($k-\epsilon$ model and the K-Omega ($k-\omega$) model. Both models seek to find the turbulent eddy viscosity by solving a set of transport equations for the turbulent kinetic energy k and the specific dissipation rate ω. The K-Omega model is typically preferred due to its better performance for boundary layers under adverse pressure gradients; it is, however, sensitive to ω values in the free stream, an aspect that is not present in the K-Epsilon model. The SST (shear stress transport) $k-\omega$ model, used later in the segment model setup, offers a variant of the $k-\omega$ model where a K-Epsilon model is applied in the far-field free stream with a K-Omega model applied near the wall.

2.5.2 The solid volume

Star-CCM+ uses the finite element method to discretise the continuous space domain of the solid into elements defined by shape functions, for instance the tetrahedral shape function, which is later used in the segment model. The solid mechanics which characterise the solid volume are defined, similarly to the fluid volume, by the conservation of mass and momentum. The solid displacement of the structure represents a combination of rigid body motion and solid deformation.

The position of a material point within a finite element in the deformed configuration is expressed as:

$$\mathbf{x}(\mathbf{X}, t) = \mathbf{X} + \mathbf{u}(\mathbf{X}, t) \tag{2.16}$$

where X is the material point position in the undeformed configuration and $u(\mathbf{X}, t)$ is the displacement between the two points.

A deformation gradient tensor F, which measures how the deformation changes from point to point, is then used to define the tensors used for stress and strain assessments.

3

Methodology and simulation models

The purpose of this chapter is to present the methodology used to develop the global riser model in OrcaFlex and the procedure used to determine the segment of interest in OrcaFlex. The selected segment model is then developed in Star-CCM+ using the environmental, physical, and dynamic properties of the segment in OrcaFlex.

3.1 Global riser model

The global riser modelling methodology covers multiple steps and is summarised in Figure 3.1. Once the riser model reaches its final configuration, the riser segment selection methodology follows another set of steps, summarised in Figure 3.2.

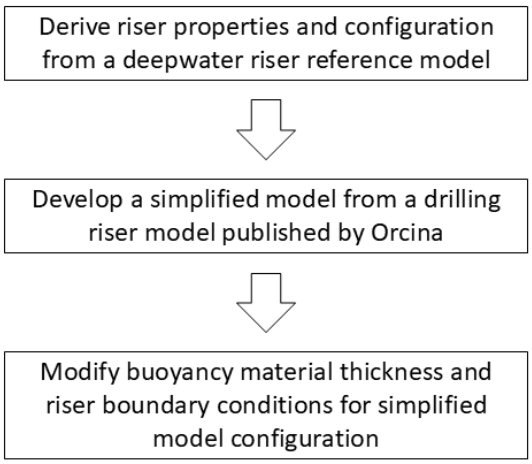

Figure 3.1: Modelling methodology steps in OrcaFlex

3.1.1 Structural model

OrcaFlex is an offshore industry specific software from Orcina frequently used to simulate the structural response of complex systems that combine the environmental

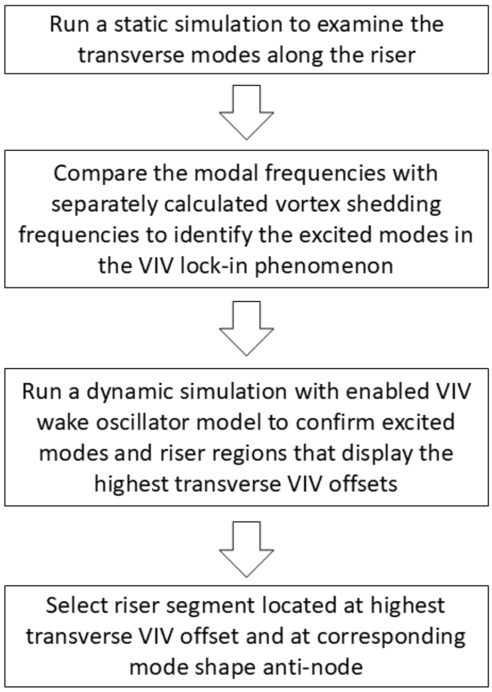

Figure 3.2: Riser segment selection methodology in OrcaFlex

effects of wind, waves, and current forces on surface vessels, as well as on connected lines and risers. Building a industry representative model in this software requires knowledge of the configuration of drilling risers, which can either be acquired based on real riser data or on previous research. Due to customer privacy agreements and limitation of use of ongoing project data, Kongsberg Maritime was not able to provide detailed configuration data for this thesis.

However, the research paper *Drilling Riser Analysis During Installation of a Well-head Equipment*, published by Sevillano et al. (2013) in the ASME 32nd International Conference on Ocean, Offshore and Arctic Engineering (OMAE 2013), specifies data for a drilling riser of 2000 meter length with buoyancy modules. The riser model in OrcaFlex reflects the overall configuration of this publication including placement of the buoyancy modules and other components, as shown in Figure 3.3.

It must be understood that the riser above is in the installation mode with the BOP hovering over the seabed. The thesis model assumes that the riser is the operating mode with the BOP sitting on the seabed. The difference in operational mode determines the values of the riser parameters, as well as the components used. For instance, the spider and gimbal, which are normally used to support the riser weight during installation and retrieval, have been omitted from the model and replaced with a tensioner system and an upper flex joint. Both configurations apply tension and allow some degree of rotational stiffness at the top end of the riser; however, the rotational stiffness provided by the gimbal is considerably higher than the flex joints. In the referenced model, the gimbal provides 600 $kN \cdot m/degree$ rotational

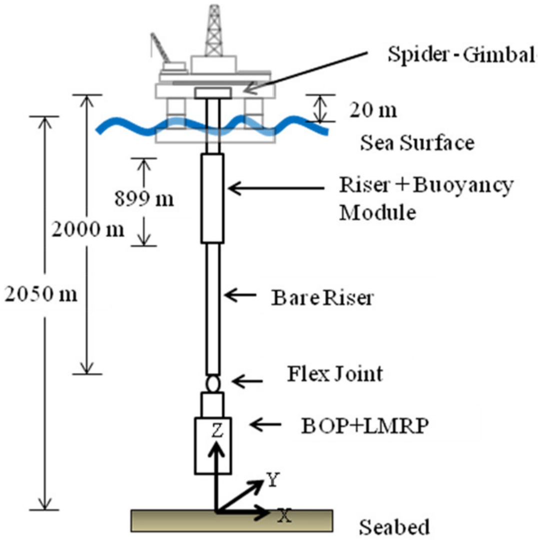

Figure 3.3: 2000-meter riser configuration

stiffness compared to 56.5 $kN \cdot m/degree$ lower flex joint stiffness. The referenced model does not provide a specific rotational stiffness value for the upper flex joint. Instead, due to the simplified nature of the drilling riser model, the lower flex joint rotational stiffness value is applied to upper flex joint as well.

The global riser model skeleton is developed using an available drilling riser model provided on the Orcina website (Orcina, 2026) then subsequently simplified to isolate the required components for an analysis of vortex induced vibrations due to current. The Orcina model consists of a 1000-meter riser with a drill string, as well as choke and kill lines, descending from a floating semi-submersible platform. For the purpose of this thesis, the auxiliary lines and the semisub are removed, along with any wave or wind interaction. The components of the model can be visualised in Figure 3.4.

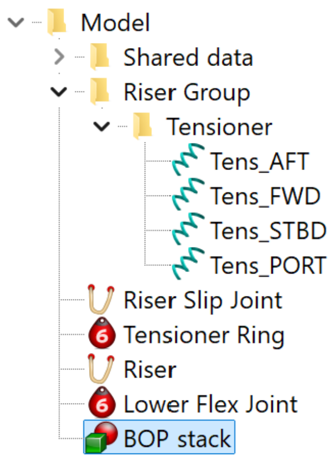

Figure 3.4: List of riser components in OrcaFlex

A set of four tensioners, shown in Figure 3.5, are each fixed at the top end and connected to the tensioner ring at the bottom end. The slip joint, which typically serves as the telescoping joint to absorb heave and other motions in the z-direction, is fixed at the top end and also connects to the tensioner ring.

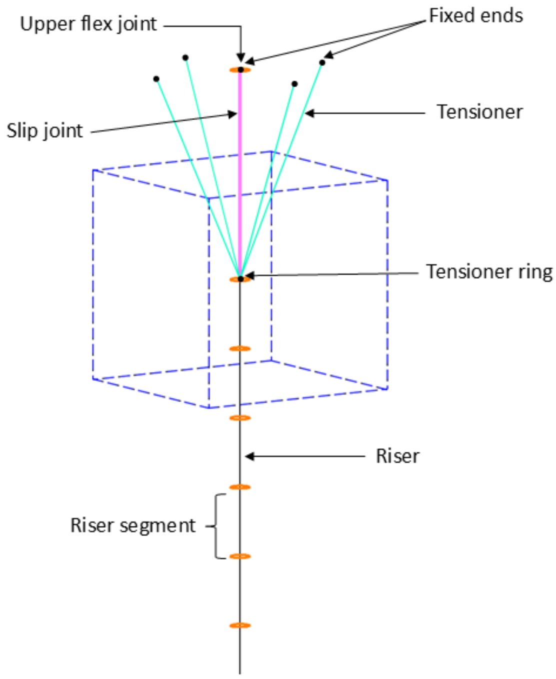

Figure 3.5: Drilling riser top tensioning system in OrcaFlex

The drilling riser connects to the tensioner ring at its top end and to to the lower flex joint at its bottom end. The lower flex joint is fixed to the BOP stack which sits on the seabed. The riser is further divided into three sections from the top end: 91 m of bare riser, 899 m of riser with buoyancy modules, and 1010 m of bare riser. The riser properties are summarised in Table 3.1.

Table 3.1: Main data for 2000-meter drilling riser

Parameter	Unit	Bare Riser	Riser with Buoyancy Modules
Outer Diameter	m	0.5343	0.8743
Inner Diameter	m	0.4889	0.4889
Linear Mass in Air	kg/m	286.4	436.9
Young's Modulus	GPa	210	210
Poisson Ratio	–	0.3	0.3
Bending Stiffness	kN·m^2	2.51×10^5	2.51×10^5
Axial Stiffness	kN	7.66×10^6	7.66×10^6

The buoyancy modules have a thickness of 0.17 m and a density of 400 $kg/m3$. Such a density is typical of syntactic foam buoyancy modules installed in deepwater environments (Matrix composites & engineering, 2026). The riser material is high strength low alloy steel, commonly used in offshore oil and gas applications, with a density of 7850 $kg/m3$ and an intrinsically high yield strength of 448 MPa.

In the drilling riser model, there are two representative flex joints, one installed at the bottom on the BOP and the other one at the top end of the slip joint. The lower flex joint rotational stiffness value, shown in Table 3.2, is derived from the referenced research paper (Sevillano et al., 2013), and is applied to the top flex joint as well. The slip joint is assigned a very low axial stiffness and high bending stiffness to enable the axial motion during the simulation (Orcina, 2026).

Table 3.2: Other components

Component	Unit	Value
Flex Joint Stiffness	kN·m/degree	56.5
Slip Joint Stiffness	kN (axial)	1
Tensioner Stiffness	kN/m	3000

3.1.2 Top tension requirement

To ensure that the tensioning system delivers the top tension to support the riser, a minimum top tension value must be calculated. Palfy (2017) defines the minimum top tension of a drilling riser as "the minimum top tension required to prevent global buckling of the riser in the event of the sudden loss of pressure in a tensioner or tensioner pair." Equation 3.1 for the minimum slip ring tension and Equation 3.2 for the minimum top tension, which can also be found in the API RP-16Q American Petroleum Institute's Recommended Practice for the Design, Selection, Operation and Maintenance of Marine Drilling Riser Systems, outline the method used to calculate the riser minimum top tension.

$$T_{SR_{\min}} = W_s f_{wt} - B_n f_{bt} + A_i \left(d_m H_m - d_w H_w\right) \tag{3.1}$$

The riser steel submerged weight is given by $W_{\mathrm{s}} = gL_r \left(m'_{\mathrm{steel}} - \rho_w \frac{\pi}{4} D_o^2\right)$ where m'_{steel} is the dry mass of the riser.

The net buoyancy material uplift is given by $B_{\mathrm{n}} = gL_b \left(\rho_w \frac{\pi}{4} D_b^2 - m'_{\mathrm{buoy}}\right)$ where m'_{buoy} is the dry mass of the buoyant material. The last component is the submerged weight of the drilling fluid, where $A_i = \frac{\pi}{4} D_i^2$.

$$T_{\mathrm{MIN}} = \frac{T_{SR_{\min}} N}{R_f (N - n)} \tag{3.2}$$

The values used in the above equations are summarised in Table 3.3. The tolerance factors and the reduction factor are estimated based on the suggestions given by Palfy (2017).

Table 3.3: Summary of variables used in minimum tension calculations

Variable	**Unit**	**Definition**	**Value**
L_r	m	steel riser length	2000
L_b	m	buoyant section length	899
f_{wt}	–	weight tolerance factor	1.05
f_{bt}	–	buoyancy tolerance factor	0.96
d_m	kg/m^3	drilling fluid density	1500
H_m	m	drilling fluid column	2000
d_w	kg/m^3	seawater density	1025
H_w	m	seawater column	1974
m'_{steel}	kg/m	riser dry mass	286.4
ρ_w	kg/m^3	seawater density	1025
D_b	m	buoyant section outer diameter	0.8743
D_o	m	outer diameter	0.5343
m'_{buoy}	kg/m	buoyancy dry mass	150.5
D_i	m	inner diameter	0.4889
N	–	number of tensioners	4
n	–	number of failed tensioners	1
R_f	–	reduction factor	0.95
g	m/s^2	gravitational acceleration	9.81

The minimum slip ring tension value $T_{SR_{\text{min}}}$ is 6.90 MN and the minimum top tension value T_{MIN} is 9.68 MN.

The tensioner system is composed of four distributed tensioners oriented at a six degree angle towards the tensioner ring. Orcina's original riser model has a non-linear tensioner system, but to simplify the model and allow easier modification of the riser top tension, a linear stiffness is used.

To ensure that the minimum riser tension criterion is satisfied, the tensioner linear stiffness is calibrated based on the effective tension at the top of the riser. In OrcaFlex, the effective tension is defined as $T_e = T_w - (p_i a_i - p_o a_o)$, where $p_i a_i$ represents the internal pressure effect, $p_o a_o$ represents the external pressure effect, and T_w is the wall tension. In this case, the external pressure is zero at the top of the riser, and the internal pressure is zero as well. Therefore, the top tension is considered equivalent to the effective tension at the top of the riser. The effective tension along riser length is plotted in Figure 3.6 with a top tension value of 9955 kN, approximately 10 MN, which is considered acceptable.

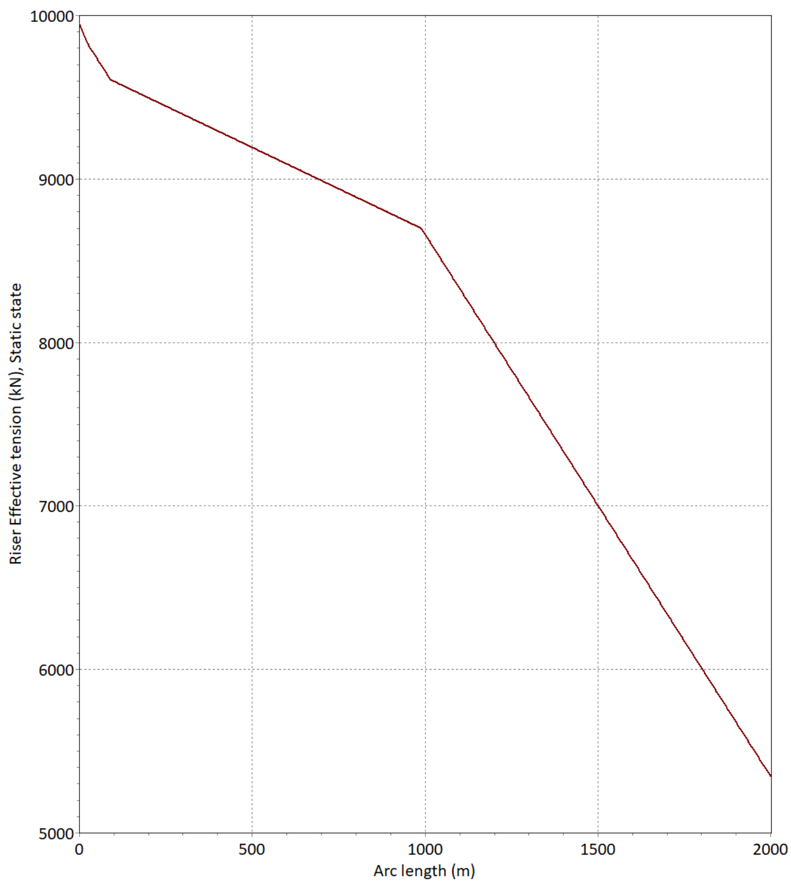

Figure 3.6: Riser effective tension plot

The tensioner force is defined as $F_t = k\,(L - L_0)$ where k is the tensioner stiffness set to 3600 KN/m, L is the stretched length equal to 4.9 m in the static state , and L_0 is the unstretched length set to 4 m.

3.1.3 Modal analysis

The objective of the modal analysis is to evaluate the excited modes and associated modal frequencies that pertain to the structural configuration of the riser model. The modal behaviour changes with the selected riser parameters, which is why it is important to first ensure the top tension parameter is accurately assessed. The modal analysis is carried out once the riser model is in the static state in which the system reaches a force equilibrium without motion. For the baseline model, the current velocity profile is set to a uniform profile of 0.6 m/s, which causes the riser to bend slightly in the x-direction, as seen in Figure 3.7.

The lock-in phenomenon represents a vibrational state in which the vortex shedding frequency is pulled towards the structure's natural frequency, and it is typically characterised by large motion amplitudes and an unchanged shedding frequency with respect to velocity fluctuations. The Strouhal relation is expressed as $f_s = St\frac{U}{D}$ where St is the Strouhal number, U is the current velocity, and D is the

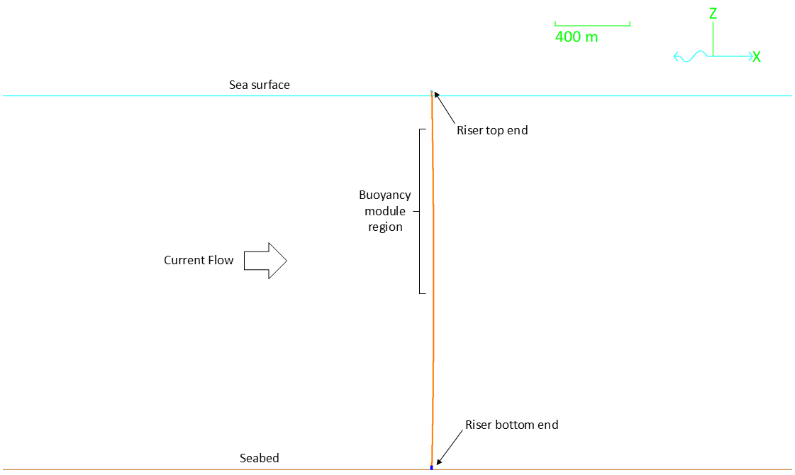

Figure 3.7: Riser configuration in the static state

outer diameter of the structure. The Strouhal number for a smooth cylinder in the subcritical flow regime can be estimated at a value of 0.2 (Potts et al., 2022). The subcritical flow regime upper bound is a Reynold's number of 10^5. The Reynold's number is expressed as $Re = \frac{UD}{\nu}$ where ν is the kinematic viscosity of seawater set to $1.36 \times 10^{-6}\,\mathrm{m^2/s}$ for seawater at 10 °C. The Reynold's number for the bare riser section is 2.36×10^5 and 3.86×10^5 for the buoyant section, which sits slightly above the upper bound of the subcritical flow regime.For the purpose of mode prediction, a Strouhal number of 0.2 is deemed reasonable. Using the Strouhal relation, a vortex shedding frequency of 0.2246 is calculated for the bare riser section and a shedding frequency value of 0.1373 for the buoyant section. Figure 3.8 confirms the separately calculated shedding frequency values.

Among the modal frequencies outlined in Table 3.4, mode 11 is selected as the excited mode for the buoyant section, and mode 19 is selected as the excited mode for the bare riser section. These modes are not by any means the definite excited modes of the riser in lock-in, but they provide useful information with regards to the structural natural frequencies when the riser sections enter lock-in, at which point $f_{\mathrm{shed}} = f_n$. The mode shapes can be visualised in Figure 3.9 and Figure 3.10.

Table 3.4: Transverse modal periods and frequencies

Mode number	Period (s)	Frequency (Hz)
9	9.103	0.110
11	7.498	0.133
13	6.480	0.154
15	5.610	0.178
17	5.021	0.199
19	4.476	0.223
21	4.093	0.244
23	3.719	0.269

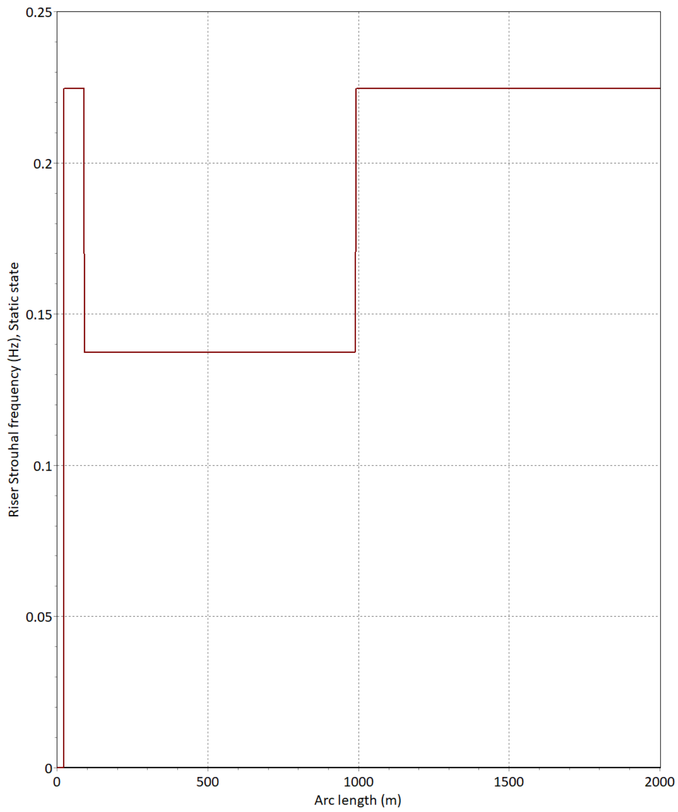

Figure 3.8: OrcaFlex riser Strouhal frequency

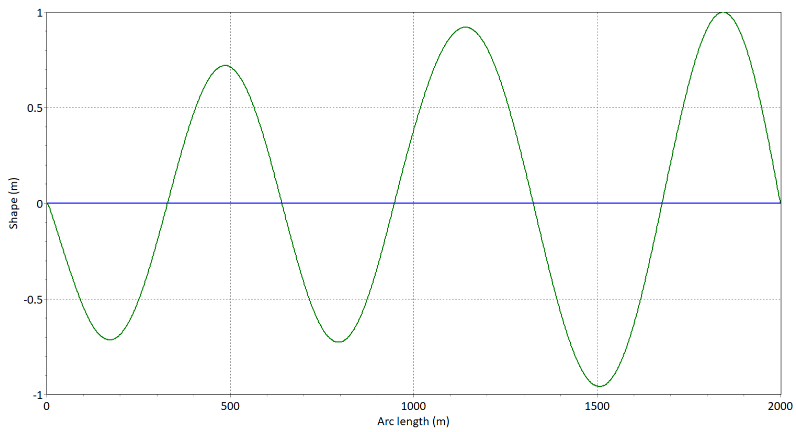

Figure 3.9: Mode shape for mode 11

3.1.4 Segment selection

The selected criterion for determining the segment of interest to model in Star-CCM+ is the transverse VIV offset, which represents the cross-flow amplitude of the riser due to vortex-induced vibrations. To assess the transverse VIV offset, an explicit time-domain dynamic simulation using the Iwan and Blevins VIV oscillator model is performed for a duration of 200 seconds, with plotted results shown in Figure 3.11.

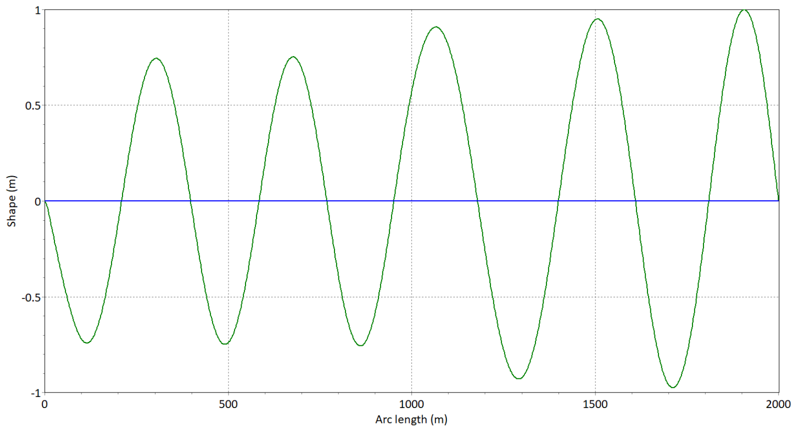

Figure 3.10: Mode shape for mode 19

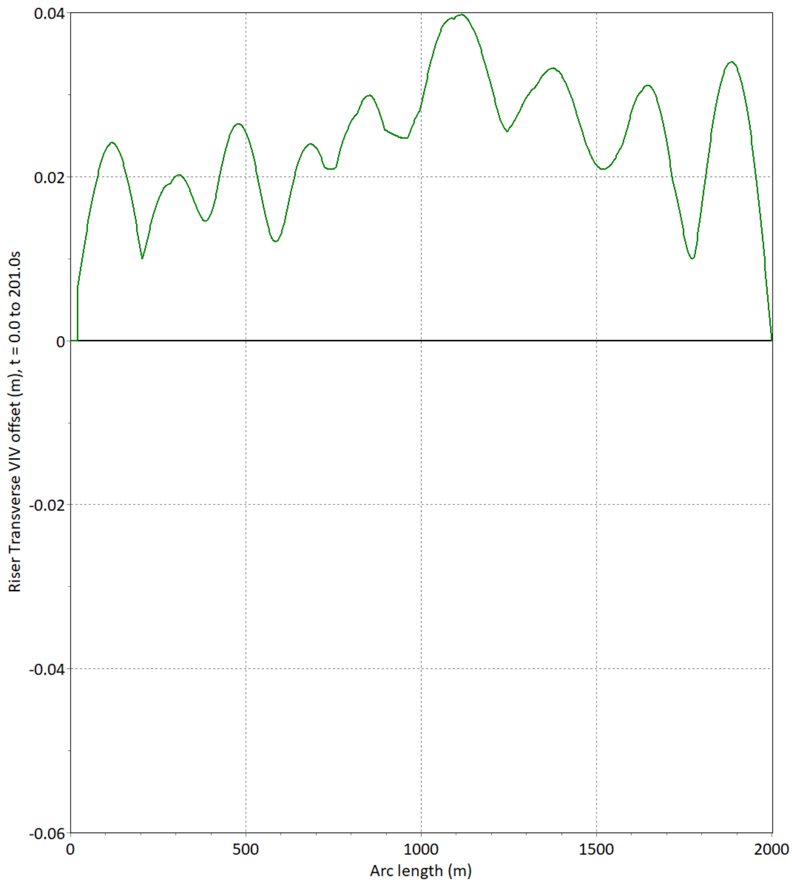

Figure 3.11: Riser maximum transverse VIV Offset

The riser displays a variation of transverse VIV offset along its length, which is caused by the multi-modal aspect of the riser. As shown in the modal analysis, the buoyancy section's excited mode in lock-in is associated with a lower modal frequency than the bare riser's excited mode. Each mode has a different mode shape, and the modes compete along the riser, which causes the variation in the transverse VIV offset. The VIV offset exhibits a maximum value at 1108 m from the top of the riser, which corresponds to the bare riser section, for which we had identified mode 19 as the excited mode in the modal analysis. Comparing the maximum value location with the anti-mode locations in Figure 3.10, it can be noted that the identified maximum VIV offset corresponds to a mode 19 anti-node at 1150 m from the top of the riser. Consequently, the segment selected for high-fidelity modelling in Star-CCM+ belongs to the bare riser section, located at 1108 m from the top of the riser.

3.2 High-fidelity segment model

3.2.1 Fluid and solid domain geometry

In Star-CCM+, the fluid domain is represented by a block part with six boundaries. Using the boolean subtract feature, the fluid domain is separated from a cylinder part with an outer diameter of 0.5343 m derived from the bare riser section outer diameter in OrcaFlex. To minimise boundary effects on the solution, the boundaries are positioned in the following manner, as shown in Figure 3.12 and Figure 3.13. The velocity inlet boundary is positioned 2.5 m, or approximately 2.5D, upstream from cylinder centre, and the pressure outlet boundary is positioned 5D downstream. The side walls, both positioned 2.5D from the cylinder centre, are assigned as slip walls which ensures that, unlike the nature of symmetry planes, they allow non-normal flow to continue downstream rather than being mirrored back into the fluid domain. The top and bottom boundaries are positioned 1D from the top and bottom ends of the cylinder, and they are assigned as slip walls as well. This fluid domain configuration is based on the fluid domain setup in a published research paper on the CFD modelling of low aspect ratio cylinders (Cajas et al., 2023). The fluid domain does not use the exact domain size as in the research paper; however, after experimenting with different boundary distances, especially regarding the side walls and pressure outlet, the current domain size was selected as the most reasonable setup with respect to the quality of vortex shedding and lack of influence of the boundary conditions on vortex formation.

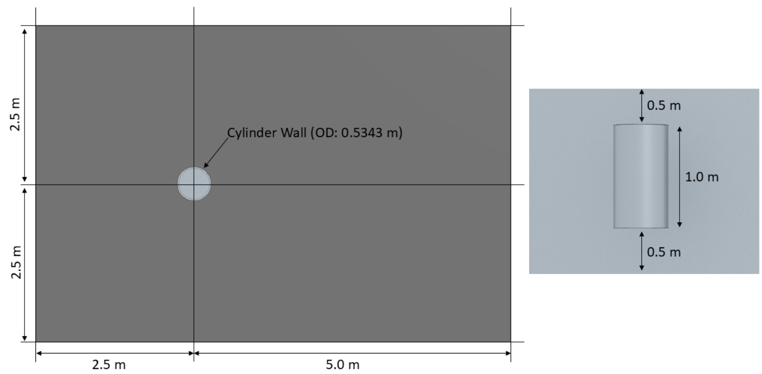

Figure 3.12: Dimensions of the fluid domain in Star-CCM+

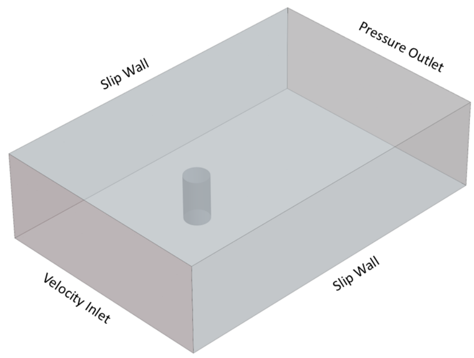

Figure 3.13: Boundaries of the fluid domain in Star-CCM+

The riser segment, represented by a computer-aided designed part created in Star-CCM+, is a short, three-dimensional pipe, with an outer diameter of 0.5343 m, an inner diameter of 0.4889 m, and a length of 1 m. The outer dimensions must match the inner dimensions of the cylinder fluid boundary to ensure a consistent fluid-structure interface between the fluid and solid domains.

3.2.2 Regions, continua, and meshing

The fluid domain is assigned to a fluid region, and the solid domain, represented by the solid pipe, is assigned to a solid region. Each region enables a different set of physics models, as shown in Table 3.5.

Table 3.5: Physics models used in Star-CCM+

Continuum	Physics Models
Physics 1 (Fluid)	Constant Density, Gravity, Implicit Unsteady, K-Omega Turbulence, Liquid, Remeshing, Reynolds-Averaged Navier-Stokes (RANS), Segregated Flow, Solution Interpolation, SST (Menter) K-Omega, Three Dimensional, Turbulent
Physics 2 (Solid)	Gravity, Implicit Unsteady, Material Law Models, Solid, Solid Stress, Solution Interpolation, Three Dimensional

The representation of the total segment mass, including the structural mass and the internal contents mass, was a technical challenge in this thesis work. To define a third separate fluid region for the drilling fluid within the inner bore of the segment also meant setting up a second fluid-structure interface, which would both increase the model's complexity and increase the simulation time. Instead, the constant density defined in the segment physics model setup represents the equivalent density of the drilling fluid and the structural steel within the segment wall thickness, allowing the internal fluid inertia to be counted with the segment inertia, and is calculated as follows:

$$A_s = \frac{\pi}{4}\left(D_o^2 - D_i^2\right) \tag{3.3}$$

$$A_f = \frac{\pi}{4} D_i^2 \tag{3.4}$$

$$\rho_{eq} = \frac{\rho_s A_s + \rho_f A_f}{A_s} \tag{3.5}$$

$$\rho_{eq} = \frac{7850(0.03648) + 1500(0.18773)}{0.03648} = 15560 \text{ kg/m}^3 \tag{3.6}$$

where A_s and A_f are the cross sectional areas for the steel and drilling fluid respectively, ρ_s is the steel density of 7850 kg/m^3, and ρ_f is the drilling fluid density of 1500 kg/m^3.

Besides the equivalent constant density of 15560 kg/m^3, the Poisson ratio is kept at 0.3, and the Young's modulus is 210 GPa. The adverse effect of the equivalent density modelling decision is that it has a small, yet important effect on the segment's fatigue life, since the higher inertia contributes to higher stresses within the segment's wall thickness. However, in this thesis, the focus is on the fluid-structure interaction, rather than the induced stresses and fatigue, so this equivalency method is considered acceptable. If the purpose were to model the stresses and fatigue, the equivalent density would be put into question, and the internal contents would need to be modelled differently.

The computational fluid domain is discretised using a predominantly polyhedral mesh with local mesh refinement applied around the cylinder wall and wake mesh refinement downstream of the cylinder. The solid domain is discretised using a tetrahedral mesh. The mesh configuration is shown using a plane section in Figure 3.14.

3.2.3 Fluid-structure interface and segment boundary conditions

To allow the fluid and structure to interact and exchange data, a mapped-contact fluid-structure interface is created between the solid and fluid regions. Such an interface requires a strong contact surface between the cylinder outer diameter and the segment outer diameter, which is set up using the boolean imprint operation.

The segment boundary condition configuration is one of the most important steps in the model development because it dictates to what extent the segment responds to the flow which has a direct impact on vortex formation. Due to the riser's high axial stiffness, the segment's motion in the axial direction is excluded in this model with the top and bottom ends of the segment being constrained in the axial direction.

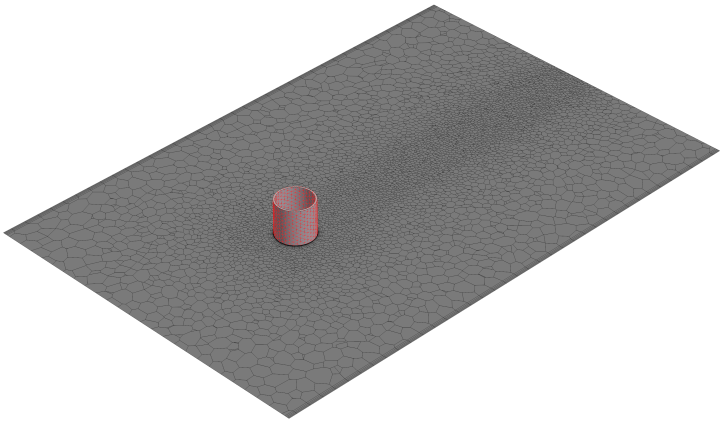

Figure 3.14: Mesh in Star-CCM+

The segment's motion is defined by two degrees of freedom in the lateral planes, and the segment is elastically supported in both x and y at the top and bottom ends, as shown in Figure 3.15, to represent the lateral bending stiffness of the overall riser at the top and bottom of the segment.

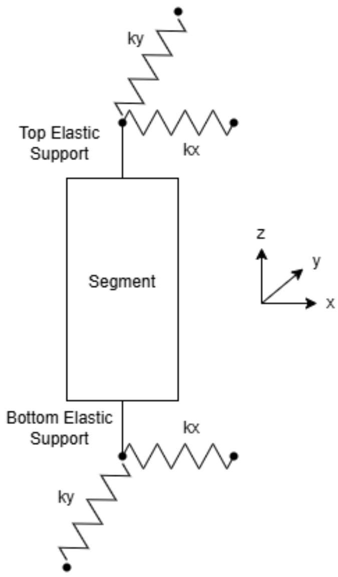

Figure 3.15: Segment elastic supports

In subsection 2.2.3, we defined the 2-DOF uncoupled matrix form on the left-hand side of Equation 2.5, which represents the structural supports of the cylinder. Here, the top and bottom elastic supports are defined as field functions in a force vector representation shown in Equation 3.7 where the off-diagonal terms are zero.

$$\mathbf{F} = \left(-\frac{k_x}{2}\,u_x - \frac{c_x}{2}\,v_x,\ -\frac{k_y}{2}\,u_y - \frac{c_y}{2}\,v_y,\ 0 \right) \tag{3.7}$$

In this equation, the structural forces are uncoupled: the force in the x-direction does not depend on the force in the y-direction and vice versa.

We earlier defined the structural system as 2-DOF uncoupled. Alternatively, the structural system can be written as two independent 1-DOF systems, as follows:

$$m_1\ddot{x}_1 + c_1\dot{x}_1 + k_1x_1 = F_L(t) \tag{3.8}$$

$$m_2\ddot{x}_2 + c_2\dot{x}_2 + k_2x_2 = F_D(t) \tag{3.9}$$

The stiffness values k_x and k_y are derived from the stiffness-frequency relation for a simple harmonic 1-DOF oscillator given by Equation 3.10; further simplified, the stiffness is calculated using Equation 3.11.

$$\omega = \sqrt{\frac{k}{m}} \tag{3.10}$$

$$k = m(2\pi f)^2 \tag{3.11}$$

As discussed earlier in subsection 3.2.2, the segment physical properties are derived from the riser model in OrcaFlex. In a similar manner, the modal frequency corresponding to the segment's excited structural mode, mode 19 in this case, is derived from the modal analysis in OrcaFlex with a value of 0.24434 Hz.

It is important to differentiate the modal frequency, modal stiffness, and modal mass from the structural frequency, stiffness, and mass. The modal mass represents the portion of mass that vibrates at its associated modal frequency, and is therefore different from the structural mass. However, the purpose in this case is to reproduce a similar response in the segment as in the riser location. This means that we want the segment to vibrate at the same frequency as the specific riser location without forcing the segment frequency to match the riser's response frequency. Instead, we match the segment's structural frequency to match the riser's natural frequency, derived from the modal analysis, closest to its vortex shedding frequency. This approach ensures that the segment displays an equivalent stiffness to match the riser's natural frequency. Since the segment's stiffness is calculated using a "matched" frequency, the modal frequency of the riser does not have to be scaled down for the segment stiffness.

However, the mass of the segment must include not only the structural and the mass of internal contents, but also the hydrodynamic added mass to account for the additional stiffness required to counteract the added inertia.

$$m_{\text{steel}} = \rho_{\text{steel}} \frac{\pi}{4} \left(\{ D_o^2 - D_i^2 \right) L \tag{3.12}$$

$$m_{\text{internal}} = \rho_{\text{internal}} \frac{\pi}{4} D_i^2 L \tag{3.13}$$

$$m_{\text{added}} = C_a \, \rho_{\text{fluid}} \frac{\pi}{4} D_o^2 L \tag{3.14}$$

$$m_{\text{total}} = m_{\text{steel}} + m_{\text{internal}} + m_{\text{added}} = 797.5 \;\; kg \tag{3.15}$$

where $\rho_{\text{steel}} = 7850 \;\; kg/m^3$, $\rho_{\text{internal}} = 1500 \;\; kg/m^3$, $\rho_{\text{fluid}} = 1025 \;\; kg/m^3$, $D_o = 0.5343 \;\; m$, $D_i = 0.4889 \;\; m$, $L = 1 \;\; m$, and $C_a = 1.0$.

Using Equation 3.11 and the calculated mass and derived modal frequency, the stiffness is calculated as shown below.

$$k = 797.5 \, (2\pi \times 0.24434)^2 \tag{3.16}$$

$$k = 1571.71 \, \text{N/m} \tag{3.17}$$

In the undamped modal analysis in OrcaFlex, each mode shape is associated with a modal frequency that has transverse and inline components. Therefore, the transverse and inline modal frequencies are identical, which is typical of symmetric systems. The stiffness k is thus applied to both k_x and k_y.

The model needs to also consider the structural and hydrodynamic damping effect of the rest of the riser, which is derived from performing a free decay test in OrcaFlex, plotted in Figure 3.16 from an initial position of 0.001 m in the y-direction from the riser's unperturbed position, and using the logarithmic decrement, denoted δ, to calculate the damping ratio of the surrounding structure in the transverse direction. The logarithmic decrement method was derived from the NTNU marine dynamics course compendium (Carl M. Larsen, 2024).

$$\delta = \frac{1}{N} \ln \left(\frac{y_n}{y_{n+N}} \right) \tag{3.18}$$

where n is the index of a peak, N is the number of cycles between the two peaks, y_n is the amplitude at peak n, and y_{n+N} is the amplitude N cycles later.

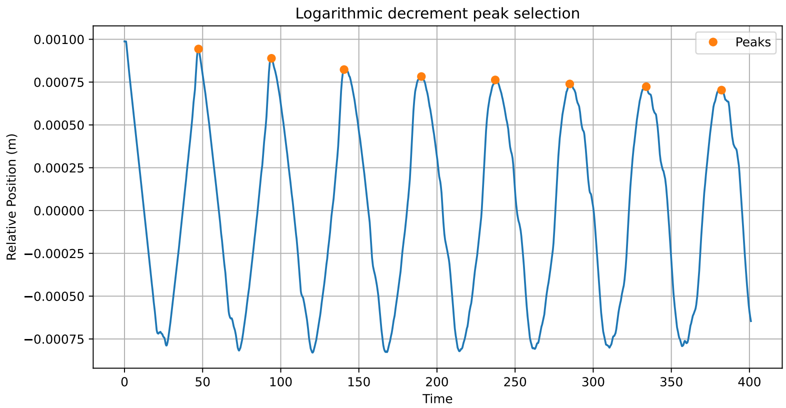

Figure 3.16: Free decay test and logarithmic decrement peak selection

The mean of the logarithmic decrements between peaks is taken to calculate the damping ratio defined for lightly damped systems as $\zeta \approx \frac{\delta}{2\pi}$.

$$\zeta \approx \frac{0.04197}{2\pi} = 0.00668 \tag{3.19}$$

The damping coefficient is derived from the standard second order system formulation $m\ddot{x} + c\dot{x} + kx = 0$ and expressed in Equation 3.20.

$$c_y = 2\zeta\sqrt{km} \tag{3.20}$$

where the mass m is the total mass, including the added mass, used earlier to find the segment's support stiffness.

$$c_y = 2 \times 0.00668\sqrt{1571.71 \times 797.5} = 14.96 \ \ \mathrm{N \cdot s/m} \tag{3.21}$$

The same method is applied in the inline direction to estimate the damping coefficient c_x, but the results are found to be almost identical; therefore, the damping coefficient c_x and c_y are given the same values. The field function for the top and bottom ends of the segment can then be expressed as shown in Equation 3.22.

$$\mathbf{F} = \left(-\frac{1571.71}{2}\,u_x - \frac{14.96}{2}\,v_x,\ -\frac{1571.71}{2}\,u_y - \frac{14.96}{2}\,v_y,\ 0\right) \tag{3.22}$$

3.3 Simulation setup

3.3.1 OrcaFlex

The simulation in OrcaFlex begins with a static simulation in which the system attempts to achieve static equilibrium given the forces due to current and the weight of the riser. Once the statics is complete, the dynamic simulation begins using an explicit time domain solution method in which the solver uses a semi-implicit Euler scheme with a constant time step to compute the equations of motion in the system from the initial static state. The time step is automatically set by OrcaFlex at the beginning of the simulation.

The Iwan and Blevins wake oscillator model used to reproduce vortex-induced vibrations in the riser, as well as other wake oscillator models, require the use of the explicit time domain method because it is a strongly coupled, dynamic system which works more efficiently when aligned with the step-by-step evolution of the explicit solver. In this setup, the default values of the Iwan and Blevins wake oscillator are retained, as recommended by Orcina (Orcina, 2025), shown in Table 3.6. In addition, the Iwan and Blevins model is defined conceptually in Equation 3.23.

$$\ddot{q} + a_0\dot{q} + a_1 q + a_2 q^3 + a_3 \dot{q}^3 = a_4 \ddot{y} \tag{3.23}$$

Table 3.6: Iwan and Blevins wake oscillator model parameters

Symbol	**Description**	**Value**
a_0	Linear damping coefficient	0.48
a_1	Linear restoring coefficient	0.44
a_2	Non-linear stiffness coefficient	0.20
a_3	Non-linear damping coefficient	0.00
a_4	Coupling coefficient	0.38
St	Strouhal number	0.20
q_0	Initial value of wake oscillator variable	0.10

The values of the Iwan and Blevins wake oscillator model are derived from experimental observations of cylinder vibration and lock-in behaviour.

3.3.2 Star-CCM+

The simulation in Star-CCM+ uses an implicit unsteady solver, which is a solution method used for transient simulations that involve turbulent models. Unlike the explicit method explained earlier in OrcaFlex, the implicit unsteady method solves the flow equations at each time step using unknown future values and iterates internally until the solution converges. For the purpose of fluid-structure interaction, the segment model must use the implicit unsteady solver for both the fluid and solid continua. The time step must be selected carefully with a second order temporal discretisation to improve the response of the transient response predictions.

Besides the system solver, the solid stress solver uses a backward differentiation second order integration method, and the mesh morpher solver allows the fluid mesh to deform smoothly according to the segment's structural motion. The mesh morpher allows for small mesh deformations, and it is required for fluid-structure interaction simulations; however, remeshing must be disabled because the mesh cannot deform and remesh simultaneously, which is a limitation when large structural motion is involved. To capture the complex flow features of FSI, the $SST\ \ k-\omega$ turbulence model is used, which creates a balanced, accurate representation of the turbulent flow near walls and in the free stream. To enable the solvers to act in each region, the motion specification must be set to solid displacement in the solid region and set to morpher in the fluid region. The fluid-structure iterative solver forms the link between the solid and fluid solvers via the FSI interface created in the structural setup.

The FSI interface spans the entire length of the segment. However, the vortex shedding and instabilities created by flow over and across the top and bottom ends of the segment can influence the lift coefficient of the segment to the point where the lift coefficient is not representative of the actual lift generated by the straight profile of the segment alone. Therefore, a threshold derived part was created in Star-CCM+ that limits the FSI interface within a specified segment span for a Z position between 0.2 m and 0.8 m of the total segment length. To ensure that results were consistent with the defined threshold section, the lift coefficient monitor reference values were specified as 1025 kg/m^3 for the reference fluid density, 0.6 m/s for the reference velocity, and 0.32058 m^2 for the reference area defined as the product of the evaluated segment length, in this case 0.6 m, and the segment outer diameter of 0.5343 m.

3.4 Data extraction and analysis

The simulation data from both OrcaFlex and Star-CCM+ is exported as a CSV file and post-processed using Python in Jupyter Lab. In Star-CCM+, the lift coefficient and cross-flow displacement are reported and plotted as the simulation runs. In OrcaFlex, the cross-flow displacement can be plotted; however, the lift coefficient must be calculated separately in Jupyter Lab using the transverse vortex force using Equation 3.24.

$$C_L = \frac{F_T}{\frac{1}{2}\rho U^2 DL} \tag{3.24}$$

To produce comparable and quality-driven representations, the response metrics including the RMS lift coefficient and RMS cross-flow displacement are post-processed and plotted in Jupyter Lab, as well as the Fourier frequency transforms utilised to assess the dominant frequencies from the lift coefficient and cross-flow displacement signals.

The RMS (root-mean-square) displacement is computed using Equation 3.25 and the RMS lift coefficient is computed using Equation 3.26. The RMS metric represents the vibrational energy of the signal, which provides a better representation of the signal's strength and makes it more suitable for comparison between the two models.

$$y_{\text{RMS}} = \sqrt{\frac{1}{N}\sum_{i=1}^{N}(y_i - \overline{y})^2} \tag{3.25}$$

$$C_{L,\text{RMS}} = \sqrt{\frac{1}{N}\sum_{i=1}^{N}\left(C_{L,i} - \overline{C_L}\right)^2} \tag{3.26}$$

The discrete fast fourier transform for a sample set of data is computed using Equation 3.27.

$$X_k = \sum_{n=0}^{N-1} x_n\, e^{-i2\pi kn/N} \tag{3.27}$$

where:

- X_k is the complex Fourier coefficient at frequency bin k,
- x_n is the sampled signal value at sample index n,
- N is the total number of samples,
- n is the time-domain sample index,
- k is the frequency-bin index,
- i is the imaginary unit satisfying $i^2 = -1$.

The frequency bin f_k expressed in Equation 3.28 is a discrete frequency value of the spectrum, and the dominant frequency is calculated as $f_{\text{dom}} = f_{k_{\text{max}}}$.

$$f_k = \frac{k}{N\Delta t} \tag{3.28}$$

- f_k is the frequency corresponding to frequency bin k,
- k is the frequency-bin index,
- N is the total number of samples,
- Δt is the sampling interval between consecutive samples.

4

Results

The methodology presented in chapter 3 is used to configure the drilling riser analysis primary baseline case, which represents a 0.6 m/s uniform current velocity profile with 9.955 MN applied top tension. Before extracting results, a mesh sensitivity analysis and segmentation sensitivity analysis are conducted in Star-CCM+ and OrcaFlex respectively. The purpose of this preliminary sensitivity analysis in both models is to ensure that the models are refined sufficiently enough to capture the physics of VIV: once the selected parameters remain relatively unchanged in increased refinement, the mesh or segment length can be deemed sufficiently refined for reliable simulation results.

Following the sensitivity analysis, the optimal setup of both models is used to run the simulations in the primary baseline case. The structural response to vortex-induced vibrations is evaluated in OrcaFlex at 1108 m from the top of the riser, since this is the location that exhibits the highest amplitude in the modal region corresponding to mode 19. In parallel, the simulation results for the developed fluid-structure interaction model in Star-CCM+ are presented. Furthermore, the two models are tested in equivalent velocity and tension conditions in a sensitivity analysis to confirm whether the results agree in varying conditions. Four parameters, including the RMS cross-flow displacement, RMS lift coefficient, dominant response frequency, and dominant lift frequency, are used to represent the simulation results and together form the basis of comparison discussed in greater detail in chapter 5.

4.1 Star-CCM+ mesh sensitivity

For accurate results and optimised simulation duration, a mesh sensitivity was conducted in Star-CCM+, and it was performed first in the fluid domain and later in the solid domain. While keeping the solid mesh base size fixed at 0.5 m (3980 cells), the fluid mesh was run through four cases going from coarse to extra fine, as Table 4.1 summarises. The sensitivity response parameters were selected based on the important VIV metrics, which include the cross-flow displacement and the dominant response and lift frequencies. Since the segment motion is both in the transverse and in-line directions, the mean drag was also included as a sensitivity response parameter.

To evaluate the effect of solid mesh refinement, the solid mesh base size is reduced

Table 4.1: Mesh sensitivity study results

Parameter	Coarse	Medium	Fine	Extra Fine
Total cell count	29561	63117	157112	293237
Base size (m)	0.5	0.3	0.2	0.2
Surface/Volumetric/Wake Refinement	0.1	0.06	0.04	0.03
Timestep (s)	0.05	0.05	0.05	0.05
Y-displacement Maximum (m)	0.048	0.043	0.076	0.124
Dominant response frequency (Hz)	0.2	0.2	0.2	0.2
Dominant lift frequency (Hz)	0.2	0.2	0.2	0.2
Mean Drag	0.597	0.604	0.577	0.660

from 0.5 to 0.1 m, which represents a cell count of 123 256. Using the refined solid mesh, three cases are tested using the fine fluid mesh configuration, with results shown in Table 4.2.

Table 4.2: Effect of solid mesh refinement and time-step reduction

Parameter	Fine	Fine ($\Delta t = 0.02$ s)
Total cell count	157112	157112
Base size (m)	0.2	0.2
Surface/Volumetric/Wake Refinement	0.04	0.04
Timestep (s)	0.05	0.02
Y-displacement Maximum (m)	0.101	0.118
Dominant response frequency (Hz)	0.2	0.2
Dominant lift frequency (Hz)	0.2	0.2
Mean Drag	0.602	0.712

From these results, the most feasible and accurate mesh configuration is as follows: fine fluid mesh using a lower time step of 0.04 seconds with a solid mesh of 0.1 m base size. Lowering the time step further may help, but the difference is quite minimal compared to the nearly doubled increase in computational time. Refining the fluid mesh further also increases the computational time for little added benefit, given the unchanging dominant frequencies and a small difference in maximum cross-flow amplitude.

4.2 OrcaFlex segmentation sensitivity

In OrcaFlex, a sensitivity study was needed to evaluate the effect of higher segmentation. This quality refers to how finely the riser is discretised along its length, and it can change the behaviour of the riser due to bending and curvature mechanics. In Table 4.3, three cases from coarse to fine segmentation are evaluated in terms of the maximum cross-flow amplitude and the dominant response frequency.

The fine segmentation case gives a slightly higher amplitude and the dominant response frequency remains nearly unchanged from the medium case. Therefore, the medium segmentation of 2 m configuration was selected for analysis.

Table 4.3: Segmentation sensitivity results

Segmentation	Y-displacement Maximum	Dominant response frequency
Coarse (5 m)	0.098	0.225
Medium (2 m)	0.114	0.23
Fine (1 m)	0.116	0.231

4.3 Computational time for both models

The computational time was earlier mentioned in section 4.1 as a limiting factor in Star-CCM+ for determining the final mesh discretisation. The simulation duration was selected with the purpose of capturing a time window of steady VIV oscillations after the initial simulation transient phase. Using the final selected mesh setup, each CFD simulation required approximately 6 hours of wall-clock time on a 12-core workstation. In sensitivity cases where the VIV oscillation periods were larger, the wall-clock time was further increased to capture a sufficient number of steady VIV oscillation cycles.

In OrcaFlex, the computational time was not considered a limiting factor for the level of segmentation. Each simulation using the final selected segmentation setup required approximately 2 hours of wall-clock time on the same workstation; however, unlike Star-CCM+, the number of cores could not be specified. This was not considered a setback, though, compared to the higher computational cost in Star-CCM+.

In both simulations, the objective was to capture a large enough time window of 5 to 10 steady VIV oscillation periods. In OrcaFlex, achieving this objective was reasonable; however, in Star-CCM+, the larger VIV oscillation periods made it very time-consuming to extract reliable results from multiple simulations. A time window of 5 steady VIV oscillations in Star-CCM+ was nevertheless considered reasonable due to the comparatively steadier oscillations than the oscillations in OrcaFlex.

4.4 Results of the primary baseline simulation

The results of the baseline simulation are summarised in Table 4.4 in which the results in both OrcaFlex and Star-CCM+ can be visualised side by side.

Table 4.4: Baseline case: comparison between OrcaFlex and Star-CCM+

Parameter	OrcaFlex	Star-CCM+
RMS cross-flow displacement [m]	0.0750	0.0716
Dominant response frequency [Hz]	0.2196	0.1998
RMS lift coefficient [-]	0.3942	0.5243
Dominant lift frequency [Hz]	0.2196	0.1998

4.4.1 Cross-flow displacement and lift coefficient

In OrcaFlex, the riser cross-flow displacement, plotted in Figure 4.1a, was sampled for a duration of 50 seconds of simulation time starting at 350 seconds with the purpose of getting past the transient phase of the simulation during which the oscillations were unsteady, and the amplitude was still in a growth phase. Though the signal captures a steadier phase of the simulation, the oscillations are nevertheless unsteady yet approximately periodic in nature. The cross-flow displacement of the segment in Star-CCM+, plotted in Figure 4.1b, was sampled for a duration of 50 seconds of simulation time starting at 90 seconds, and displays a comparatively steadier, periodic oscillatory signal. The RMS metric of the cross-flow displacement is only 4.5% lower in Star-CCM+ than in OrcaFlex, as shown in Table 4.4.

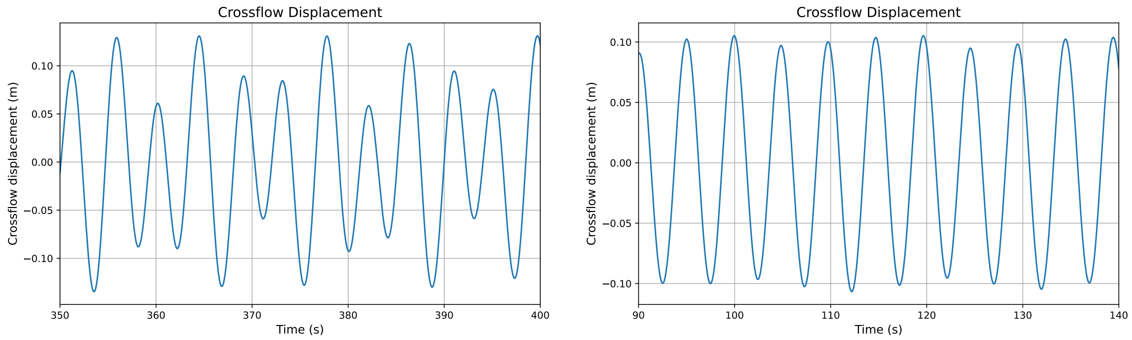

(a) Displacement in OrcaFlex

(b) Displacement in Star-CCM+

Figure 4.1: Baseline case: cross-flow displacement comparison

As discussed in section 3.4, the generated transverse vortex force in OrcaFlex was post-processed to compute the non-dimensional lift coefficient plotted in Figure 4.2a and evaluated within the same simulation time frame as the cross-flow displacement signal in Figure 4.1a. The lift coefficient in Star-CCM+, as well, is evaluated within the same simulation time frame as the cross-flow displacement in Figure 4.1b. The RMS lift coefficient metric is 33% higher in Star-CCM+ than in OrcaFlex.

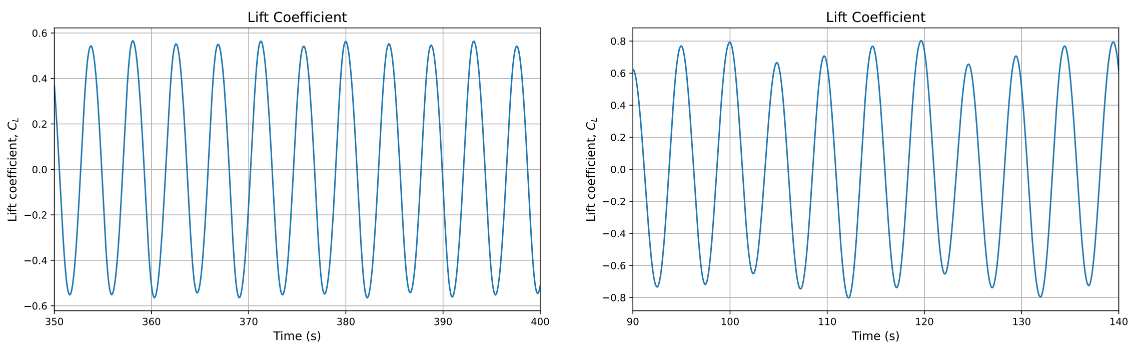

(a) Lift coefficient in OrcaFlex

(b) Lift coefficient in Star-CCM+

Figure 4.2: Baseline case: lift coefficient comparison

4.4.2 Dominant response and lift frequencies

Although the amplitude of lift and displacement are of great importance with respect to riser analysis, their respective frequencies can provide further information, namely the lock-in phenomenon and the presence of other vibration modes. The riser model model in OrcaFlex indeed exhibits a multimodal response characterised by the two peaks in Figure 4.3a. Both peaks align well with the modal analysis values estimated in chapter 3 of 0.223 Hz for mode 19 and 0.154 Hz for mode 11. In comparison, the segment model in Star-CCM+ exhibits a unimodal response, characterised by the single peak in Figure 4.3b. The difference in model behaviour is attributed to the modelling methodology. In OrcaFlex, the entire riser's response is accounted for, including the vibrational contribution of the buoyant section. In Star-CCM+, however, the model is built and tuned to the natural frequency closest to the vortex shedding frequency of the bare section. The model's response is therefore expected with only a 9% difference with the dominant frequency in OrcaFlex.

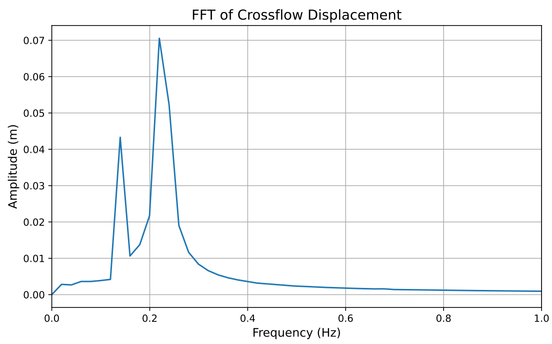

(a) Response frequency in OrcaFlex

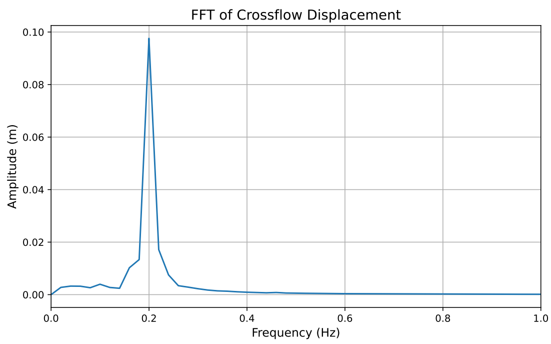

(b) Response frequency in Star-CCM+

Figure 4.3: Baseline case: dominant response frequency comparison

As for the lift frequencies shown in Figure 4.4, both signals display a single peak that align precisely with the dominant response peaks in Figure 4.3. Such a behaviour is characteristic of the lock-in phenomenon, in which the lift frequency, otherwise known as the vortex shedding frequency, locks onto the structure's dominant response frequency. This observation, along with the significant RMS cross-flow displacement, confirms that the behaviour of both models is consistent with lock-in.

4.5 Sensitivity analysis

A comprehensive sensitivity analysis was conducted to determine the behaviour of both models in varying conditions. The baseline case serves as a robust primary evaluation of model behaviour in lock-in conditions and with a uniform velocity profile. However, in realistic offshore conditions, the current velocity magnitude at the studied depth is usually lower, and the current velocity profile is not uniform in nature. Table 4.5 summarises the studied sensitivity cases.

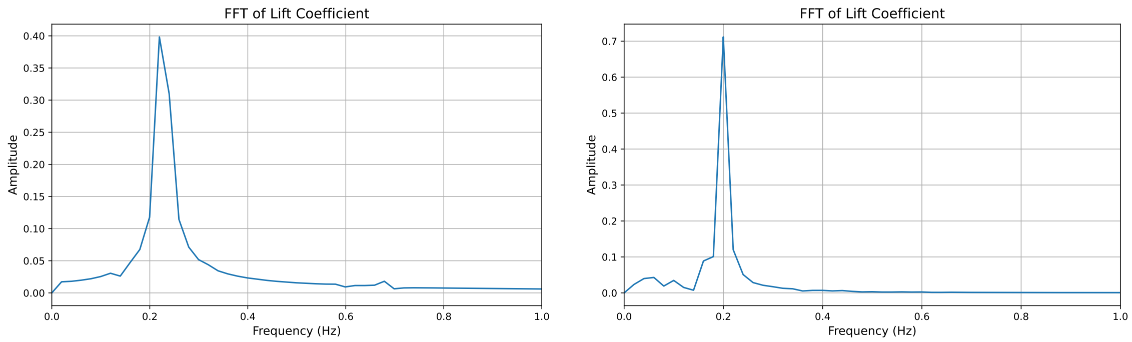

(a) Lift frequency in OrcaFlex **(b)** Lift frequency in Star-CCM+

Figure 4.4: Baseline case: dominant lift frequency comparison

Table 4.5: Sensitivity analysis cases

Case	Description	Velocity (m/s)	Top tension (MN)
Baseline	Uniform velocity profile	0.6	9.955
1	Uniform velocity profile	0.4	9.667
2	Linearly sheared velocity profile	0.6-0	9.638
3	Linearly sheared velocity profile	0.6-0	7.964
4	Linearly sheared velocity profile	0.6-0	11.946

In sensitivity cases 1 and 2, the riser model in OrcaFlex experiences a decrease in top tension, as seen in Table 4.5 due to the decrease in current velocity and current loads. In cases 2 and 4, the top tension is deliberately changed to assess the effect of top tension. In all cases, the result of the change in top tension is a change in the modal behaviour of the riser. The excited modes and modal frequencies are different, as shown in Table 4.6, and affects the derived stiffness and damping coefficients used to define the segment model's boundary conditions in Star-CCM+. The dynamic properties in Star-CCM+ are updated for each of the cases.

Table 4.6: Dynamic properties for each Star-CCM+ case

Case	Nat. Frequency (Hz)	Stiffness (N/m)	Damping coefficient
Baseline	0.22343	1571.71	14.96
1	0.15151	722.72	10.14
2	0.10765	364.85	7.21
3	0.09514	284.98	6.37
4	0.09938	310.95	6.65

The Strouhal relation is expressed as $St = \frac{f_s D}{U}$, and the reduced velocity is expressed as $U_r = \frac{U}{f_n D}$, as covered earlier in chapter 2. In lock-in conditions, $f_n = f_s$, and so the two equations can be re-written as $U_r = \frac{1}{St}$. For a Strouhal number of 0.2, the reduced velocity is 5, but realistically the Strouhal number may fluctuate during the simulation. The lock-in is likely around $U_r = 5$, but may also occur under lower or higher reduced velocities. The reduced velocity parameter is defined in Table 4.7 for each case.

Table 4.7: Reduced velocity estimation for each case

Case	Reduced Velocity	U (m/s)	D (m)
Baseline	5.03	0.6	0.5343
1	4.94	0.4	0.5343
2	4.57	0.2627	0.5343
3	5.17	0.2627	0.5343
4	4.95	0.2627	0.5343

At the beginning of each case description, a summary table of results is presented, which forms the comparison basis to evaluate the difference in results between OrcaFlex and Star-CCM+.

4.5.1 Case 1

The results of the case 1 simulation are summarised in Table 4.8 in which the results in both OrcaFlex and Star-CCM+ can be visualised side by side.

Table 4.8: Case 1: comparison between OrcaFlex and Star-CCM+

Parameter	OrcaFlex	Star-CCM+
RMS cross-flow displacement [m]	0.0547	0.0633
Dominant response frequency [Hz]	0.1499	0.1399
RMS lift coefficient [-]	0.1607	0.4452
Dominant lift frequency [Hz]	0.1499	0.1399

In case 1, the velocity profile remains uniform in OrcaFlex, but the current velocity is decreased to 0.4 m/s. In Star-CCM+, the inlet boundary condition velocity magnitude is changed to 0.4 m/s. The cross-flow displacement, plotted in Figure 4.5, displays an RMS metric in Star-CCM+ that is 15.7% higher than in OrcaFlex.

The lift coefficient, plotted in Figure 4.6, displays an RMS metric in Star-CCM+ that is 177% higher than in OrcaFlex.

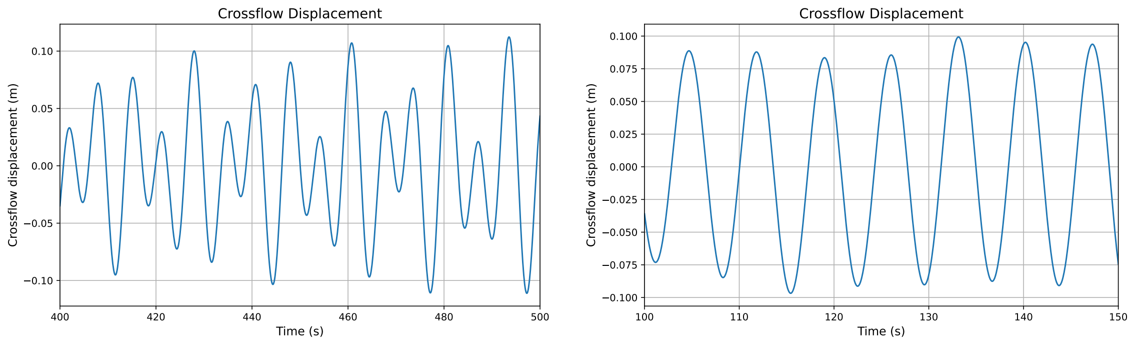

(a) Displacement in OrcaFlex **(b)** Displacement in Star-CCM+

Figure 4.5: Case 1: cross-flow displacement comparison

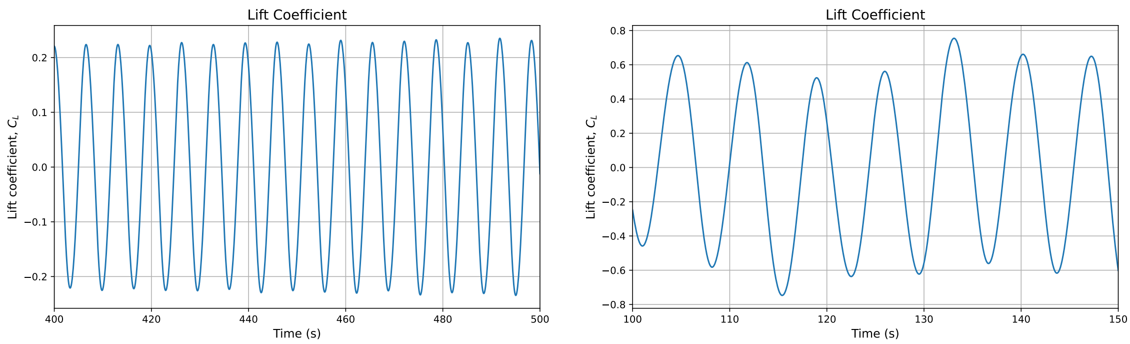

(a) Lift coefficient in OrcaFlex **(b)** Lift coefficient in Star-CCM+

Figure 4.6: Case 1: lift coefficient comparison

Similarly to the baseline case, the riser model in OrcaFlex exhibits a multimodal response, as shown in Figure 4.7a with lower associated frequencies than the baseline case due to the change in riser top tension. The segment model in Star-CCM+ expectedly displays a single dominant response frequency with only a 6.7% difference from the dominant response frequency in OrcaFlex.

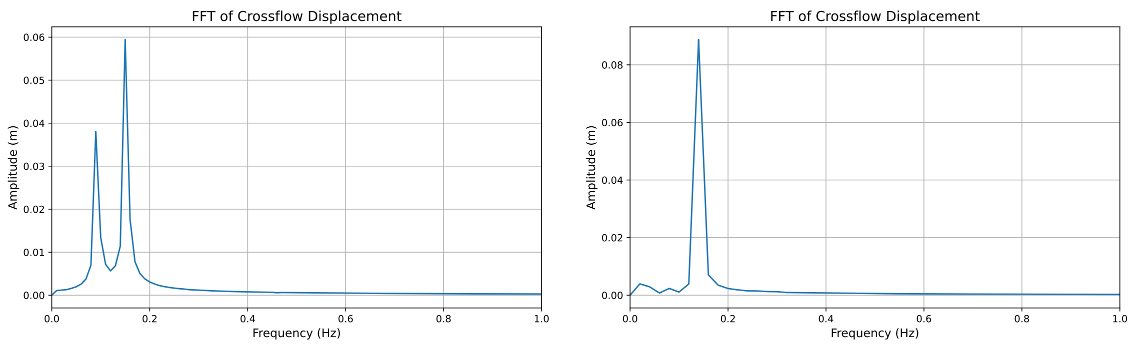

(a) Response frequency in OrcaFlex **(b)** Response frequency in Star-CCM+

Figure 4.7: Case 1: dominant response frequency comparison

The dominant lift frequency in both models, shown in Figure 4.8, is equal to the dominant response frequency. Along with the significant, relatively unchanged RMS cross-flow displacement magnitude, lock-in behaviour can be confirmed for both models.

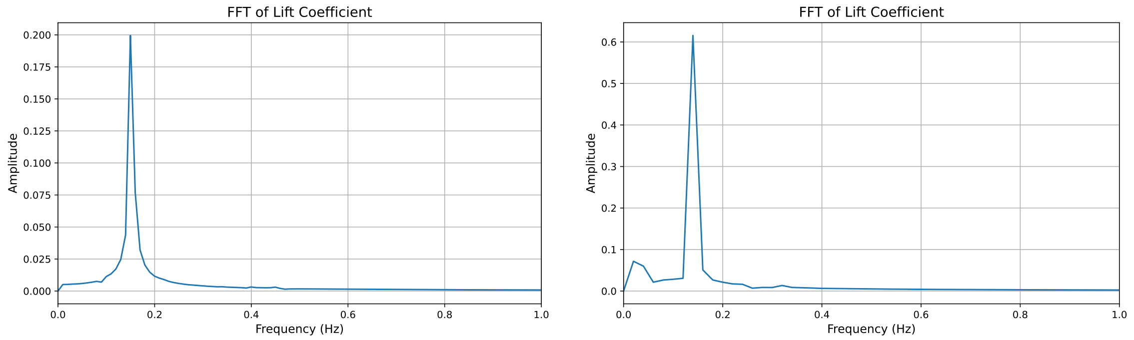

(a) Lift frequency in OrcaFlex

(b) Lift frequency in Star-CCM+

Figure 4.8: Case 1: dominant lift frequency comparison

4.5.2 Case 2

The results of the baseline simulation are summarised in Table 4.9 in which the results in both OrcaFlex and Star-CCM+ can be visualised side by side.

Table 4.9: Case 2: comparison between OrcaFlex and Star-CCM+

Parameter	OrcaFlex	Star-CCM+
RMS cross-flow displacement [m]	0.0119	0.0119
Dominant response frequency [Hz]	0.1299	0.0800
RMS lift coefficient [-]	0.0706	0.0936
Dominant lift frequency [Hz]	0.0999	0.0800

In case 2, the velocity profile is defined as linearly sheared in OrcaFlex, in which the current velocity at the surface is 0.6 m/s and decreases linearly to 0 m/s at the bottom of the riser. In Star-CCM+, the inlet boundary condition velocity magnitude reflects the local conditions of the selected segment, which requires a linear interpolation resulting in a constant span-wise velocity magnitude of 0.2627 m/s. The cross-flow displacement, plotted in Figure 4.9, displays an RMS metric in Star-CCM+ that is actually the same as in OrcaFlex.

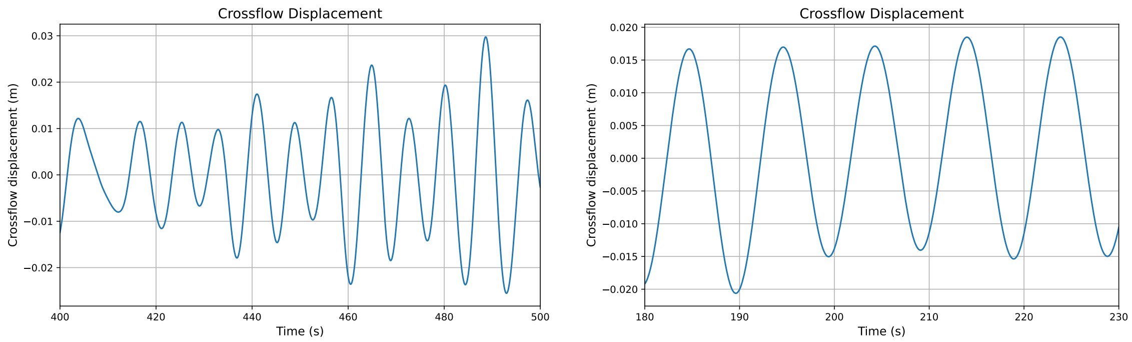

(a) Displacement in OrcaFlex **(b)** Displacement in Star-CCM+

Figure 4.9: Case 2: cross-flow displacement comparison

The lift coefficient, plotted in Figure 4.10, displays an RMS metric in Star-CCM+ that is 32.6% higher than in OrcaFlex.

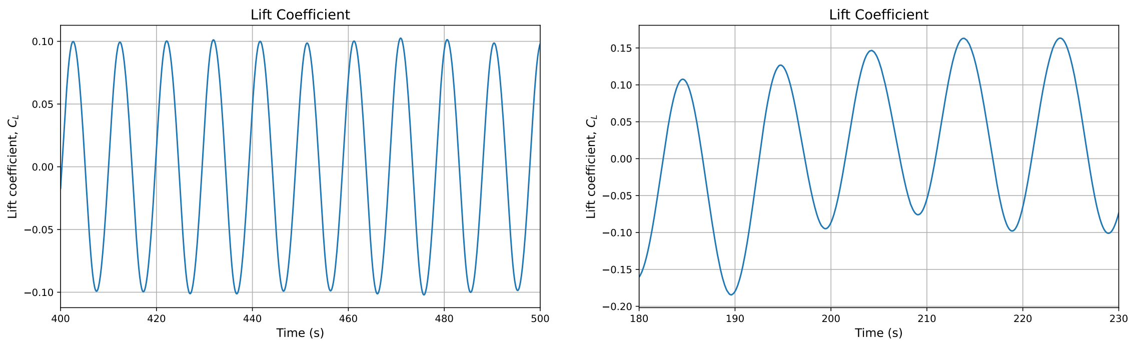

(a) Lift coefficient in OrcaFlex **(b)** Lift coefficient in Star-CCM+

Figure 4.10: Case 2: lift coefficient comparison

In contrast with the two previous cases, the riser model in OrcaFlex exhibits a nearly unimodal response, as shown in Figure 4.11a. The segment model in Star-CCM+ displays a single dominant response frequency with a 38.4% difference from the dominant response frequency in OrcaFlex.

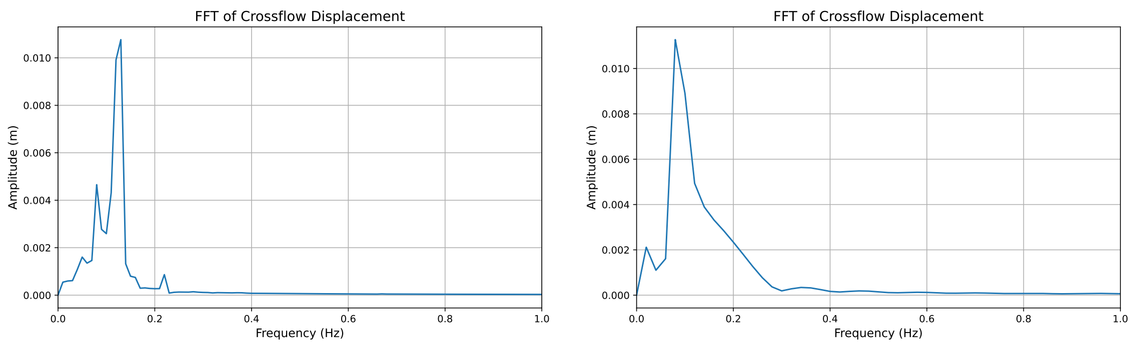

(a) Response frequency in OrcaFlex **(b)** Response frequency in Star-CCM+

Figure 4.11: Case 2: dominant response frequency comparison

The dominant lift frequency in OrcaFlex, shown in Figure 4.12a, is different from the dominant response frequency, while in Star-CCM+ it is observed that they are both equal. The segment model in Star-CCM+ is consistent with lock-in behaviour, albeit weaker lock-in due to the lower RMS cross-flow displacement magnitude, while the same cannot be said for the riser model in OrcaFlex in which the frequency synchronisation is absent. It is also worth noting in the Star-CCM+ model that, compared to the narrow dominant response and dominant lift frequency peaks in the baseline case and case 1, the peaks in case 2 are broader in nature, which may be attributed to the model's end effects.

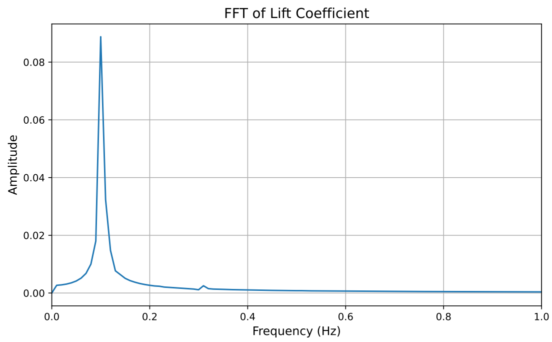

(a) Lift frequency in OrcaFlex

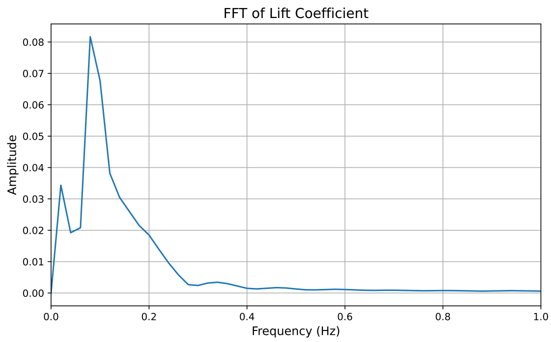

(b) Lift frequency in Star-CCM+

Figure 4.12: Case 2: dominant lift frequency comparison

4.5.3 Case 3

The results of the baseline simulation are summarised in Table 4.10 in which the results in both OrcaFlex and Star-CCM+ can be visualised side by side.

Table 4.10: Case 3: comparison between OrcaFlex and Star-CCM+

Parameter	**OrcaFlex**	**Star-CCM+**
RMS cross-flow displacement [m]	0.0086	0.1139
Dominant response frequency [Hz]	0.0999	0.0800
RMS lift coefficient [-]	0.0717	0.7367
Dominant lift frequency [Hz]	0.0999	0.0800

In case 3, the velocity profile is linearly sheared in OrcaFlex, and the riser top tension is decreased by 17% relative to the top tension in case 2. In Star-CCM+, the model still experiences an inlet velocity magnitude of 0.2627 m/s. The cross-flow displacement, plotted in Figure 4.13, displays an RMS metric in Star-CCM+ that is significantly higher than in OrcaFlex by approximately one order of magnitude.

The lift coefficient, plotted in Figure 4.14, displays an RMS metric in Star-CCM+ that is, similarly to the cross-flow displacement comparison, approximately one order of magnitude higher than in OrcaFlex.

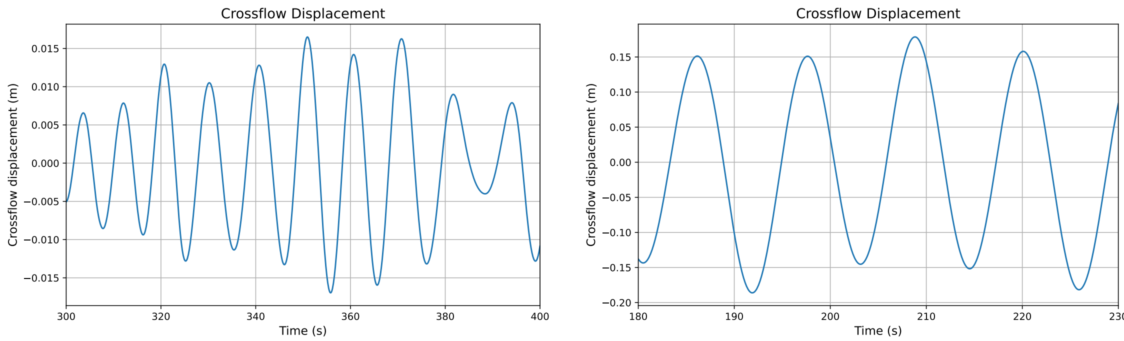

(a) Displacement in OrcaFlex

(b) Displacement in Star-CCM+

Figure 4.13: Case 3: cross-flow displacement comparison

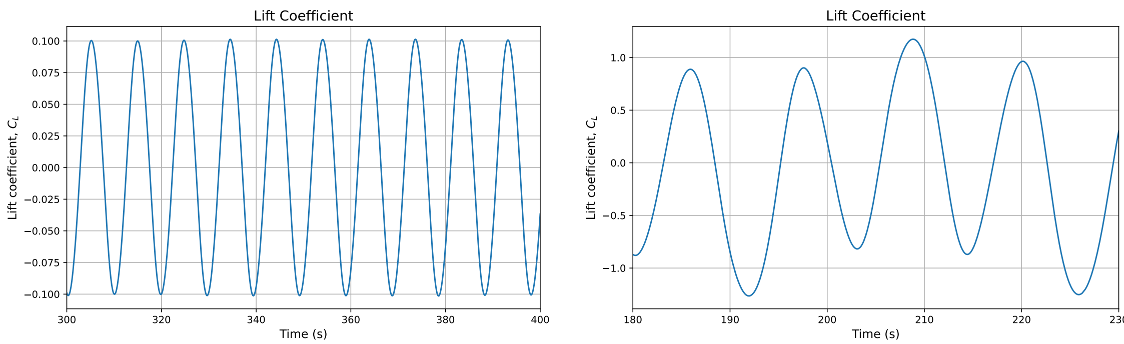

(a) Lift coefficient in OrcaFlex

(b) Lift coefficient in Star-CCM+

Figure 4.14: Case 3: lift coefficient comparison

The riser model in OrcaFlex now exhibits a completely unimodal response, as shown in Figure 4.15a. The segment model in Star-CCM+ also displays a single dominant response frequency with a 19.9% difference from the dominant response frequency in OrcaFlex.

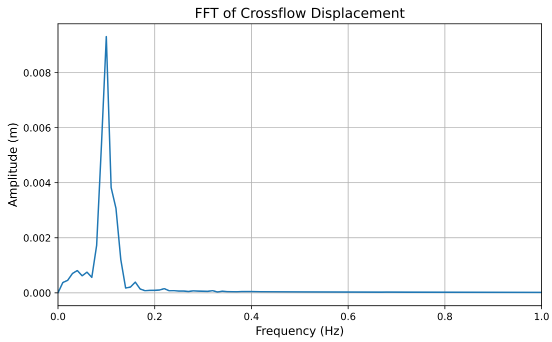

(a) Response frequency in OrcaFlex

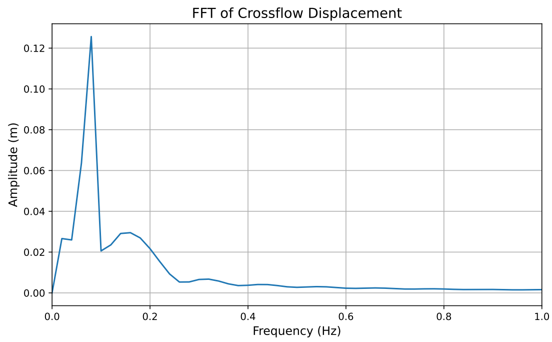

(b) Response frequency in Star-CCM+

Figure 4.15: Case 3: dominant response frequency comparison

The dominant lift frequency in both models, shown in Figure 4.16, is equal to the dominant response frequency. The behaviour of both models is consistent with lock-in, though the segment model in Star-CCM+ experiences a stronger version of lock-in due to its significantly higher RMS cross-flow displacement magnitude. It is worth noting in the Star-CCM+ model that the dominant response and dominant lift frequency peaks are quite narrow with a broadband area in the higher frequency range.

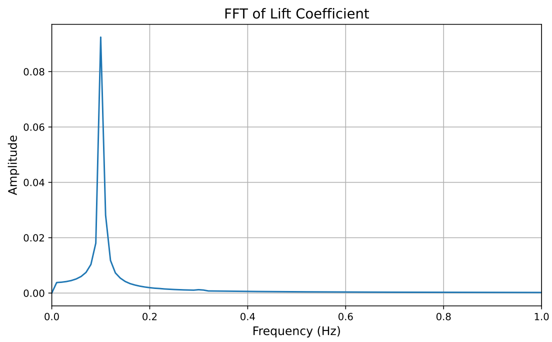

(a) Lift frequency in OrcaFlex

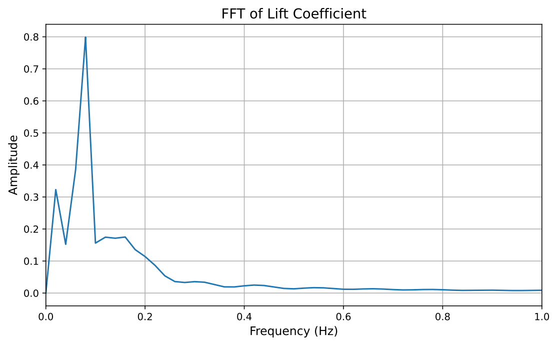

(b) Lift frequency in Star-CCM+

Figure 4.16: Case 3: dominant lift frequency comparison

4.5.4 Case 4

The results of the baseline simulation are summarised in Table 4.11 in which the results in both OrcaFlex and Star-CCM+ can be visualised side by side.

Table 4.11: Case 4: comparison between OrcaFlex and Star-CCM+

Parameter	OrcaFlex	Star-CCM+
RMS cross-flow displacement [m]	0.0122	0.0826
Dominant response frequency [Hz]	0.0899	0.0999
RMS lift coefficient [-]	0.0716	0.5652
Dominant lift frequency [Hz]	0.0999	0.0999

In case 4, the velocity profile is linearly sheared, and the riser top tension this time is increased by 19 % relative to the top tension in case 2. In Star-CCM+, the model still experiences an inlet velocity magnitude of 0.2627 m/s. The cross-flow displacement, plotted in Figure 4.17, displays an RMS metric in Star-CCM+ that is, in this case too, significantly higher than in OrcaFlex by nearly one order of magnitude.

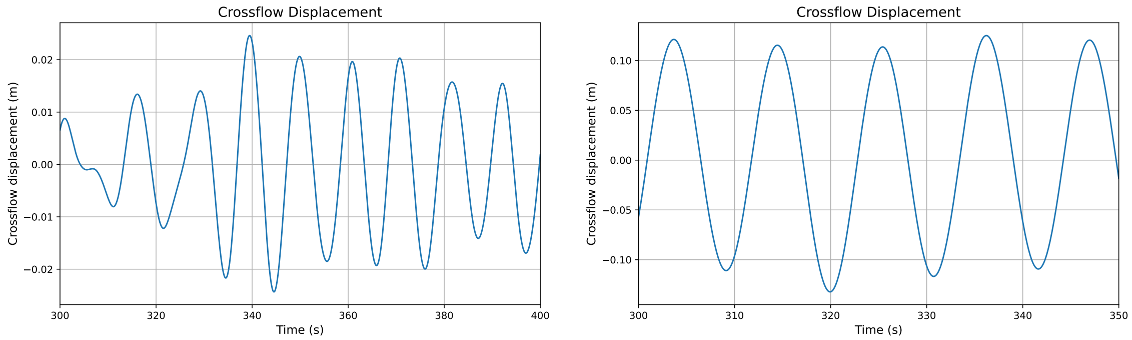

(a) Displacement in OrcaFlex

(b) Displacement in Star-CCM+

Figure 4.17: Case 4: cross-flow displacement comparison

The lift coefficient, plotted in Figure 4.18, displays an RMS metric in Star-CCM+ that is, similarly to the cross-flow displacement comparison, nearly one order of magnitude higher than in OrcaFlex.

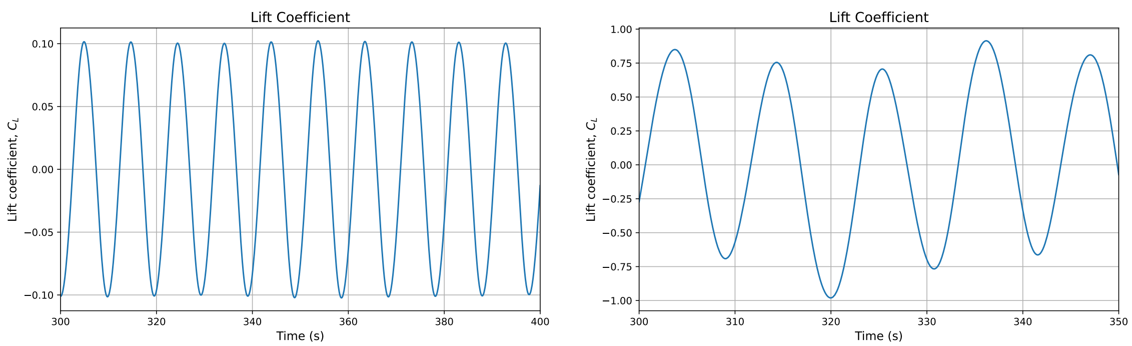

(a) Lift coefficient in OrcaFlex

(b) Lift coefficient in Star-CCM+

Figure 4.18: Case 4: lift coefficient comparison

The riser model in OrcaFlex exhibits a unimodal response, as shown in Figure 4.19a. The segment model in Star-CCM+ also displays a single dominant response frequency with an 11.1% difference from the dominant response frequency in OrcaFlex.

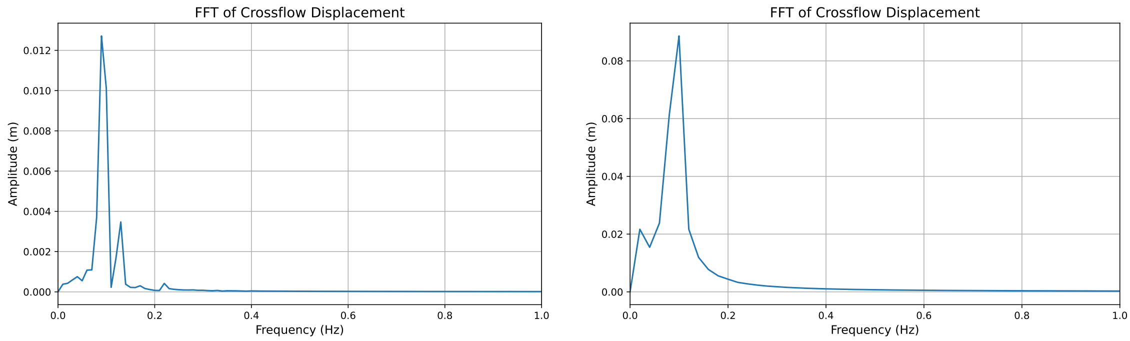

(a) Response frequency in OrcaFlex

(b) Response frequency in Star-CCM+

Figure 4.19: Case 4: dominant response frequency comparison

The dominant lift frequency in OrcaFlex, shown in Figure 4.20a, is different from the dominant response frequency, while in Star-CCM+ it is observed that they are both equal. The segment model in Star-CCM+ is consistent with strong lock-in behaviour, while the same cannot be said for the riser model in OrcaFlex in which the frequency synchronisation is absent and the RMS cross-flow displacement is low in magnitude. It is worth noting in the Star-CCM+ model that the dominant response and dominant lift frequency peaks are narrow in nature, nearly consistent with the peak characteristics of the baseline case and case 1.

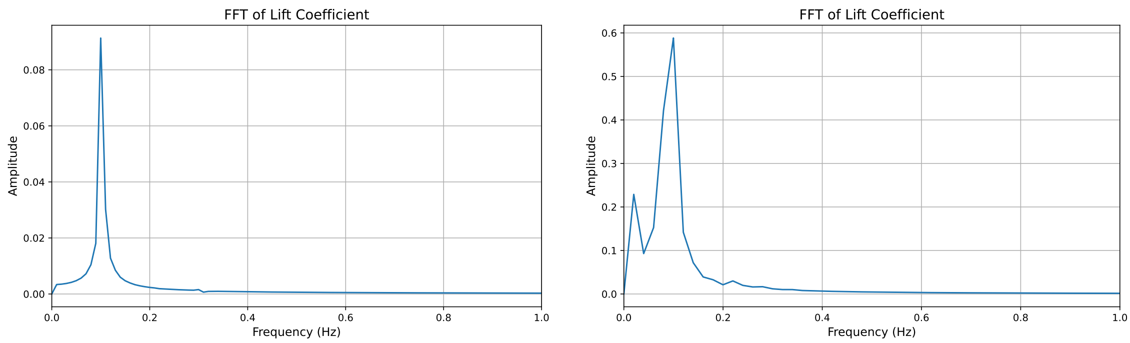

(a) Lift frequency in OrcaFlex

(b) Lift frequency in Star-CCM+

Figure 4.20: Case 4: dominant lift frequency comparison

5

Discussion

The results of the baseline simulation case have been presented and discussed briefly. However, the results from the sensitivity cases have yet to be analysed and discussed, and a comparison between the results in OrcaFlex and the results in Star-CCM+ is required to form a basis on the conditions of similarity and on the implications for riser design and analysis.

5.1 Limitations of the study

This study is limited to two degrees of freedom behaviour of the riser segment in Star-CCM+, which is not inherently different from the behaviour of the riser in OrcaFlex in which the wake oscillator primarily focuses on the transverse vortex force with an inline Morison drag force approximation. Furthermore, torsion effects are not included in OrcaFlex, which makes the two models more comparable. The two degree of freedom aspect of the Star-CCM+ model does limit the use of the model for asymmetric modelling purposes, in which the effects of rotational inertia must be considered.

5.2 Comparison between the models

5.2.1 Baseline case

Both OrcaFlex and Star-CCM+ models in the 0.6 m/s uniform case present a nearly identical RMS cross-flow displacement. The RMS lift coefficients differ, which points to a difference in coupling strength between the segment motion and the wake. Lock-in however, is achieved in both simulations, though the dominant frequencies differ. The wake behaviour in lock-in can be visualised in Figure 5.1.

5.2.2 Case 1

Both models in the 0.4 m/s uniform case exhibit similar RMS cross-flow displacements, but the RMS lift coefficients differ substantially. The fluid-structure coupling in Star-CCM+ is indeed stronger, as noted in the baseline case. The RMS lift coefficient only decreased by 15 % from the baseline case in Star-CCM+, compared to a 59 % decrease in OrcaFlex. The dominant frequencies in both models, however, are

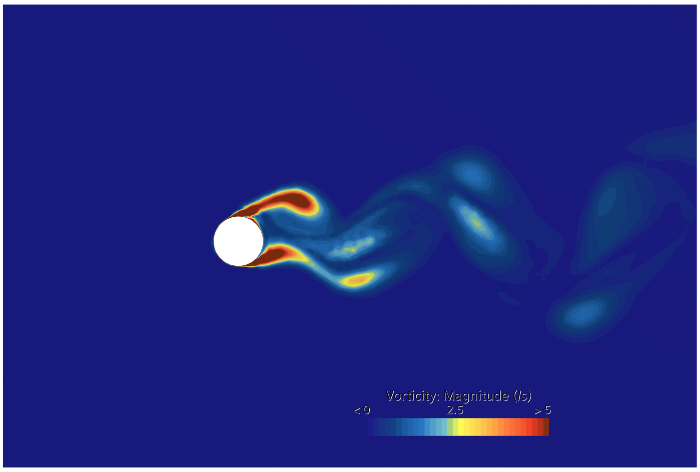

Figure 5.1: Baseline case: vortex street behind segment in Star-CCM+

much closer than in the baseline case, and both models exhibit lock-in behaviour with the matching response and lift frequencies. Figure 5.2 displays a weaker vortex formation in Star-CCM+, but the alternating vortex shedding pattern is still very visible.

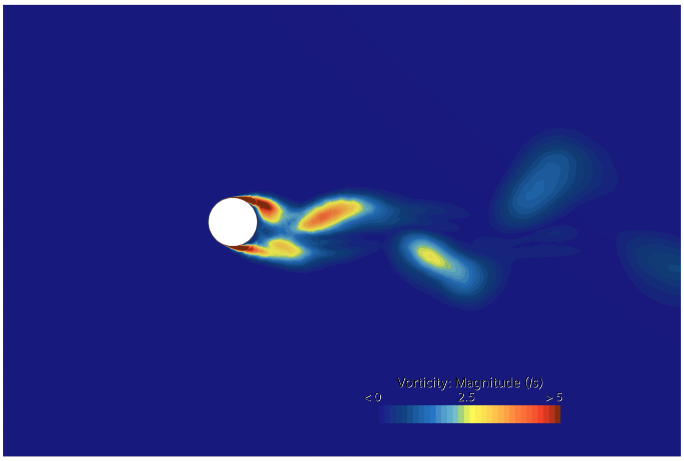

Figure 5.2: Case 1: vortex street behind segment in Star-CCM+

5.2.3 Case 2

Both models in the linearly sheared case have an identical RMS cross-flow displacement, and their RMS lift coefficients are quite similar, more so than in case 1. Their dominant frequencies, however, diverge, and an interesting aspect can be noted about the lock-in behaviour. The OrcaFlex model does not display lock-in behaviour due to the 0.2 Hz gap between the response and lift frequencies, whereas the Star-CCM+ model displays lock-in behaviour with matching frequencies. Figure 5.3 shows the weak vortex formation in Star-CCM+ without the alternating vortex shedding pattern of a segment in lock-in and a rather symmetric shedding. In chapter 4, the reduced velocity table shows a drop in reduced velocity in case 2 to a value of 4.57, which may indicate the lower bound of the lock-in range. The OrcaFlex model appears to respond faster to non lock-in conditions compared to the Star-CCM+ model.

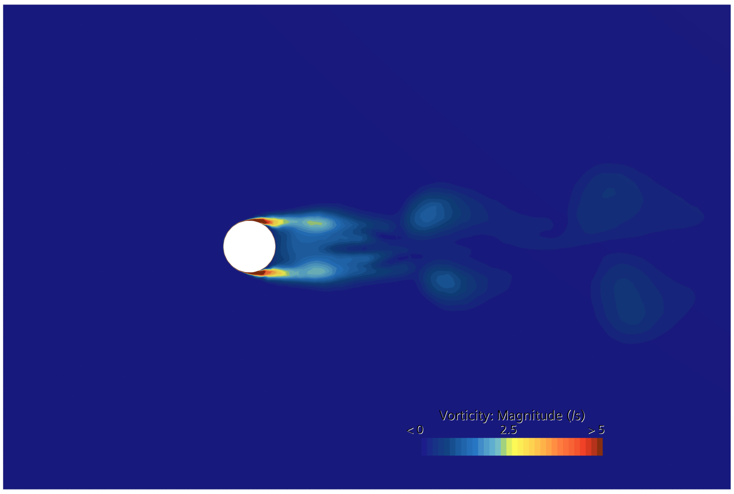

Figure 5.3: Case 2: vortex street behind segment in Star-CCM+

5.2.4 Case 3

In the linearly sheared low top tension case, it is normally expected that both models respond with higher cross-flow displacement amplitudes than in case 2, since the lack of top tension reduces the riser's effective stiffness. The Star-CCM+ model reacts accordingly with an RMS cross-flow displacement of 0.1139 m, approximately 10 times the RMS value in case 2 and larger than the RMS value in the baseline case. The RMS lift coefficients display a similar difference with an RMS value in Star-CCM+ 7 times greater than the RMS value in OrcaFlex. Both models are in lock-in, though the dominant frequencies differ. Figure 5.4 shows stronger vortex formation in the segment's wake than in case 2.

5.2.5 Case 4

In the linearly sheared high top tension case, it is expected that the higher tension would increase the riser's effective stiffness, thereby inducing lower cross-flow amplitudes. The Star-CCM+ model has an RMS cross-flow displacement 8 times greater than in case 2, and the OrcaFlex model RMS cross-flow amplitude value remains quite close to the RMS value in case 2. The RMS lift coefficient in OrcaFlex remains unchanged compared to cases 2 and 3, but the RMS value in Star-CCM+ is 5 times greater than in OrcaFlex. Overall, it appears that the OrcaFlex RMS lift coefficient and displacement do not change significantly between cases 2, 3, and 4, but in Star-CCM+ they do. However, the dominant frequencies in all cases are very similar between the two models. Figure 5.5 shows stronger vortex formation than both cases 2 and 3.

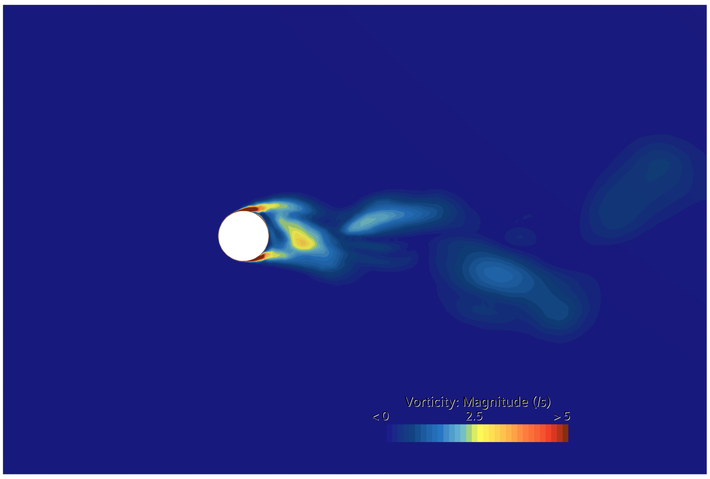

Figure 5.4: Case 3: vortex street behind segment in Star-CCM+

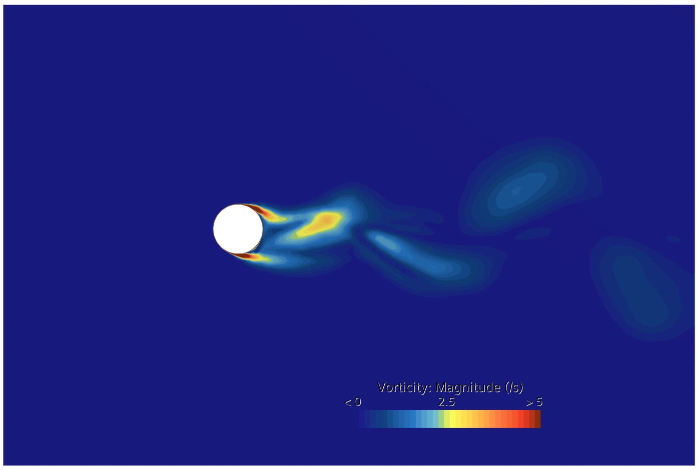

Figure 5.5: Case 4: vortex street behind segment in Star-CCM+

5.3 Overview of key findings

The following figures summarise the key findings of the sensitivity analysis by showing how each relevant parameter changes for each case.

The first key finding is that both models display very similar dominant response and dominant lift frequencies, as shown in Figure 5.6 and Figure 5.7.

The second key finding is that both models display lock-in behaviour, in which the dominant lift frequency aligns with the dominant response frequency, in all cases except for case 2. In case 2, only the Star-CCM+ model indicates lock-in, though comparatively weaker, as shown in the vortex street representation. In the lower bound of the lock-in range, OrcaFlex may not indicate lock-in, unlike Star-CCM+.

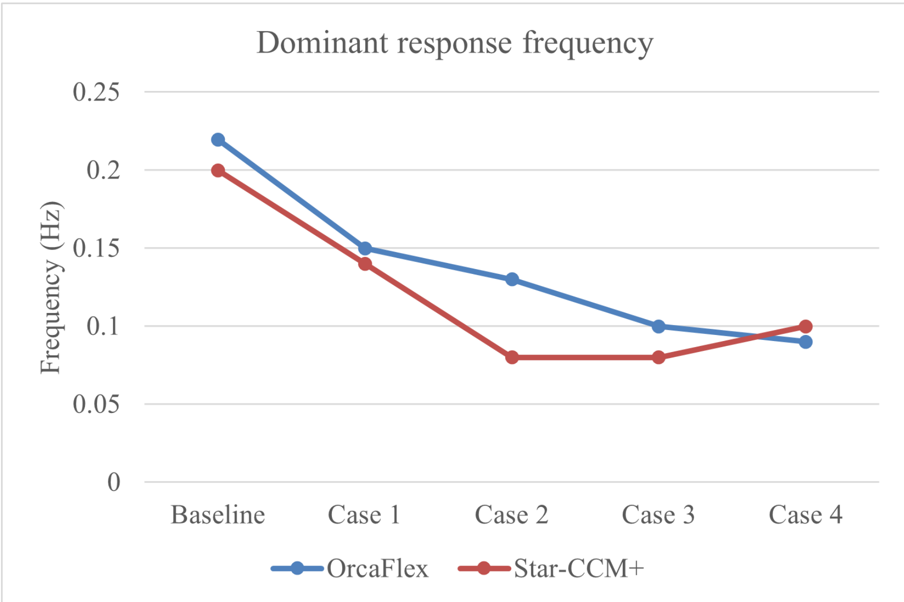

Figure 5.6: Summary of dominant response frequency for all cases

The third key finding is that the RMS cross-flow displacement and the RMS lift coefficient display a similar trend in the baseline case and cases 1 and 2. However, when the top tension is modified in cases 3 and 4, the RMS values between the two models diverge significantly from the previous trend, as shown in Figure 5.8 and Figure 5.9.

To understand why the RMS values in cases 3 and 4 are so different from case 2, Figure 5.10 can be referred to, which shows a similar trend in the reduced velocity to the trend of the RMS values in Star-CCM+. In case 3, the reduced velocity is increased significantly from case 2, which places the model in an increasingly high chance of lock-in. The lock-in behaviour and vortex formation, as shown in the vortex street representations, is much stronger in case 3 than in case 2. In case 4, though the top tension is increased compared to case 2, the reduced velocity of the model remains nearly as high as in case 3. The reduced velocity increases with decreasing natural frequency. When the top tension was increased in OrcaFlex,

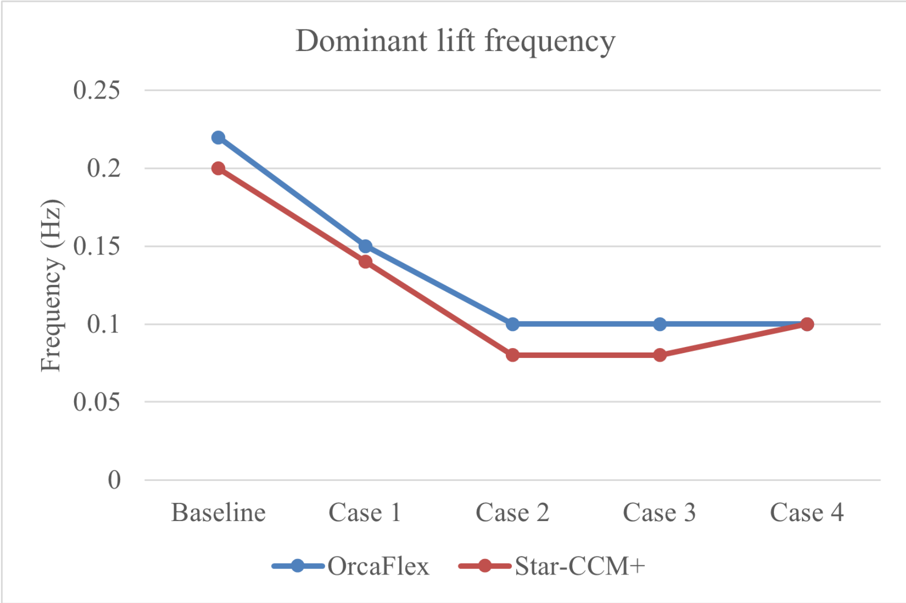

Figure 5.7: Summary of dominant lift frequency for all cases

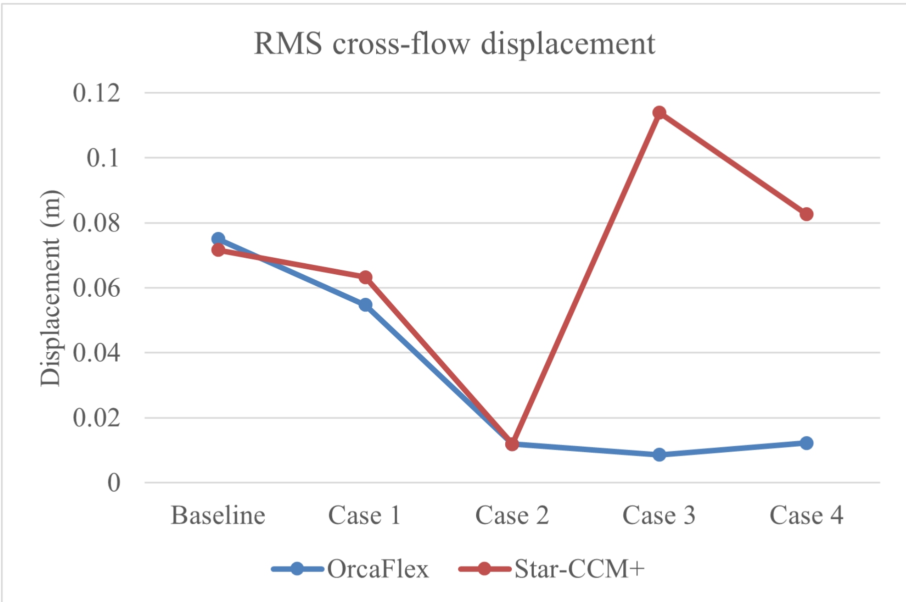

Figure 5.8: Summary of RMS displacement for all cases

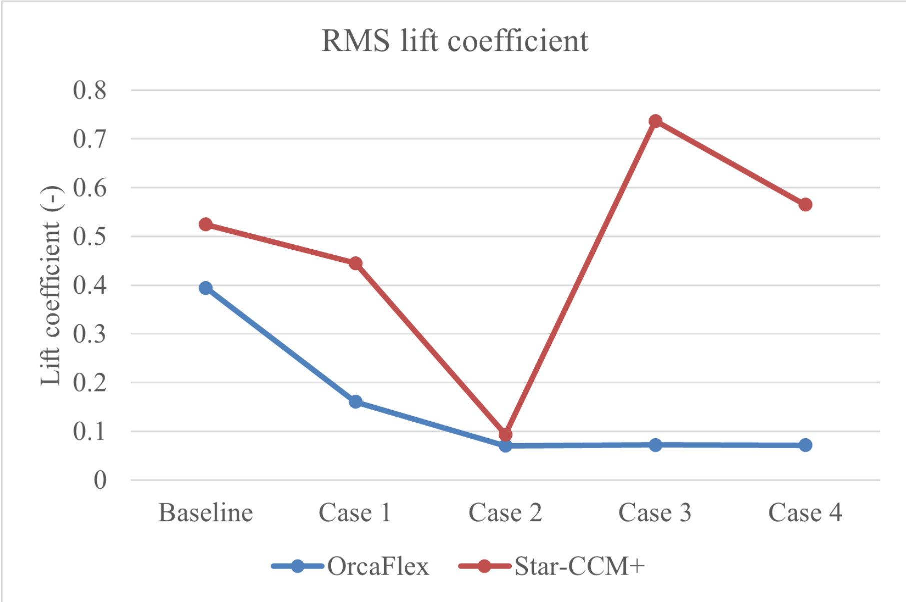

Figure 5.9: Summary of RMS lift coefficient for all cases

the modal analysis results changed, to the point where the excited mode was now associated with a lower natural frequency than in case 2. Therefore, the reduced velocity remained high as compared to the reduced velocity in case 3. As a result, both cases 3 and 4 display stronger lock-in behaviour than in case 2, which explains the divergent trend in RMS cross-flow displacement and RMS lift coefficient.

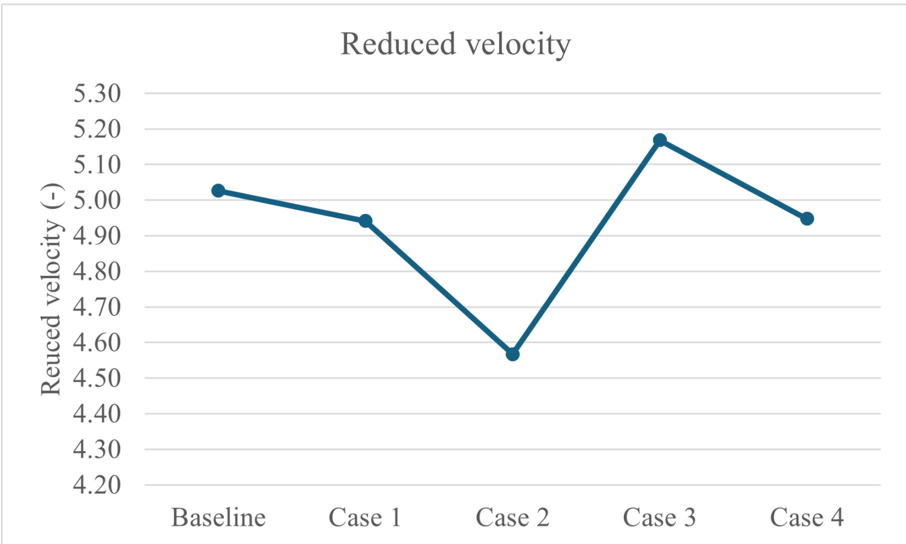

Figure 5.10: Reduced velocity U_r for all cases

5.4 Implications for riser design and analysis

The fact that the two models display similar RMS dominant frequencies and RMS lift frequencies is important for riser design and analysis for fatigue damage estimations, in which the frequency of oscillations has a direct impact on fatigue predictions. In applications where an engineer would like to estimate the effect of a VIV suppression device in Star-CCM+, the alignment of frequencies between the global riser model and the local high-fidelity model ascertains that the VIV suppression device can accurately disrupt the same vortex formation present in the global model. Furthermore, the bare riser section model may be used reliably as a baseline tool for comparison to a model with the VIV suppression device.

Similarly, the fact that the RMS cross-flow displacement and RMS lift coefficient trends align for three cases where the top tension is relatively unchanged shows that the Star-CCM+ model has similar sensitivity to changes in current velocity, but may over-predict the RMS lift coefficient due to stronger fluid-structure coupling. In addition to response frequency, fatigue estimation depends as well on the amplitude of oscillation. If Star-CCM+ can enable similar amplitude estimation with a slight over-prediction, the fatigue estimation can be carried out with more confidence.

The divergent trend of the Star-CCM+ RMS values indicates much stronger lock-in behaviour with respect to reduced velocity. The OrcaFlex model remains relatively unresponsive to significant changes in top tension. Therefore, the Star-CCM+ model is considerably more sensitive to these changes, and the results must be handled with caution because the change in top tension may induce other structural dynamic effects in OrcaFlex that dampen the response.

Due the global riser's multi-modal behaviour, the vibrational energy from the bare riser section mode may be transferred over to the lower mode associated with the buoyant section, thereby reducing the riser's response at the selected location. The dampened response in OrcaFlex may also originate from the semi-empirical wake oscillator formulation, which may artificially reduce the wake dynamics via the linear damping coefficient a_0. According to Zhang et al. (2023), the classic wake oscillator model can accurately predict VIV response of a cylinder at high mass-damping ratios, but fails to predict the VIV response accurately at low mass-damping ratios. The mass-damping ratio is expressed as $m^*\zeta$, where $m^* = \frac{m}{\rho\frac{\pi D^2}{4}}$ and ζ is the structural damping ratio. Using the combined structural and internal content mass per unit length of $567.9kg/m$, calculated earlier in chapter 3, the mass ratio $m = 2.47$, which gives a mass-damping ratio of 0.0163. This value is quite low, and may be a contributing factor to the decreased response of the full-scale riser model in OrcaFlex.

This represents an important limitation of Star-CCM+: the high-fidelity model may not be able to include all the factors that affect global riser dynamics, and therefore may over-predict RMS values in the context of complex riser dynamics. However, the wake oscillator model in OrcaFlex may also under-predict the response due to the riser's low mass-damping ratio. In such a case, the wake oscillator may need to be re-calibrated to accurately predict VIV behaviour at low mass-damping ratios. Alternatively, a modified wake oscillator model as the model proposed by Zhang et al. (2023) may be warranted for a more accurate comparison between the two models.

6

Conclusions

The purpose of this chapter is to summarise the study, present the key findings of the study, and provide a well-rounded answer to the research objectives stated in section 1.2.

6.1 Summary of the study

In this thesis, an independent, high-fidelity, two-degree-of-freedom model was developed in Star-CCM+ using the physical properties of the selected riser location in OrcaFlex. The local current velocity was estimated based on velocity at the equivalent depth, and the dynamic properties of the model, including structural support stiffness and damping coefficients, were derived from the OrcaFlex riser modal analysis for the baseline case and subsequently for each sensitivity case. The dynamic behaviour of both models was assessed with respect to RMS cross-flow amplitude, RMS lift coefficient, dominant response frequency, and dominant lift frequency.

6.2 Key findings

The key findings of the study are as follows:

1. Both models display similar dominant response and dominant lift frequencies.

2. Both models experience lock-in in most cases.

3. Both models display a similar trend in RMS cross-flow displacement and RMS lift coefficient values with respect to current velocity magnitude and profile changes.

4. The RMS cross-flow displacement and RMS lift coefficient results between the two models diverge in cases of significant top tension changes.

6.3 The research objectives

In section 1.2, the general objective was to investigate the vortex-induced vibrational response of both a high-fidelity CFD model of a short riser segment and a low-fidelity, global drilling riser model. The specific research objectives were defined as follows:

1. Develop a realistic, low-fidelity drilling riser model in OrcaFlex using a wake oscillator to simulate VIV.

2. Select a VIV-sensitive segment of the riser in OrcaFlex and develop a high-fidelity CFD model of the segment in Star-CCM+ using a two-way FSI interface.

3. Run both models under the same conditions and compare the predicted VIV amplitudes and dominant frequencies.

4. Investigate the influence of velocity profile and magnitude and the variation of riser top tension on the VIV predictions of both models.

5. Evaluate the ability of the high-fidelity CFD model to capture the local riser dynamic VIV response predicted by the low-fidelity drilling riser model.

6. Identify the strengths and limitations of the high-fidelity model and the low-fidelity model.

6.4 Answer to the research objectives

Objective 1: Development of the low-fidelity drilling riser model

The drilling riser model was developed in OrcaFlex using a drilling riser model from the software developer's website, then further simplified, and assigned physical properties from a reference model included in a published, peer-reviewed research paper.

Objective 2: Development of the high-fidelity segment model

The riser segment model was developed in Star-CCM+ with a two-way FSI interface and derived physical, environmental, and dynamic properties from the carefully selected segment location in the OrcaFlex model. The extraction of properties for Star-CCM+ implementation followed a logical, well-documented process to ensure equivalency between both models.

Objective 3: Simulation and baseline case comparison

The explicit, time-domain simulation in OrcaFlex implemented the Iwan and Blevins wake oscillator model with OrcaFlex default coefficients to simulate the VIV response. The implicit unsteady solver in Star-CCM+ was used to simulate the fluid-structure interaction between the segment and the wake. The baseline case in both simulations displayed lock-in behaviour and similar response metrics.

Objective 4: Sensitivity analysis using four cases

A comprehensive sensitivity analysis was conducted to evaluate how both models respond to changes in velocity magnitude and profile and changes in top tension. The velocity variations in cases 1 and 2 produced a similar trend in response metrics. The top tension variation, however, produced higher amplitudes in Star-CCM+, while the amplitudes in OrcaFlex remained relatively unchanged.

Objective 5: Evaluation of the high-fidelity segment model

The high-fidelity segment model performs well, and can accurately reproduce the VIV behaviour of the OrcaFlex model in different velocity conditions, though the stronger FSI coupling may in certain cases induce a stronger response. The high-fidelity segment model, however, cannot accurately reproduce the VIV behaviour of the OrcaFlex model in cases of top tension changes because it displays strong sensitivity to changes in reduced velocity. In addition, the segment model's dynamic properties are tied to a specific modal frequency, which does not consider the multi-modal behaviour of the full-scale riser.

Objective 6: Strengths and limitations of the high-fidelity model and the low-fidelity model

By explicitly resolving the flow field, the high-fidelity model can accurately capture the physics of vortex shedding and FSI coupling effects. In doing so, however, it remains highly sensitive to changes in reduced velocity, and can predict stronger amplitudes during lock-in. Furthermore, the model's lock-in behaviour is tied to its simplified structural vibration dynamics, which cannot capture the full-scale riser's multi-modal response. In contrast, the low-fidelity model can efficiently model the full-scale riser and capture global structural dynamics. It is considerably more computationally efficient than the high-fidelity model. However, the wake oscillator model used relies on a semi-empirical formulation, which can dampen the lock-in response, because it does not explicitly resolve vortex shedding.

6.5 Final remarks

Overall, the study demonstrated that high-fidelity modelling of short riser segments can reproduce the relevant vortex-induced vibrational response metrics of the deep-water drilling riser model in OrcaFlex for different current velocity profiles, but it cannot reliably reproduce the changes in global riser dynamics in different top tension conditions. Determining whether the difference in response between the two models is attributed to the high-fidelity segment model's inability to capture complex riser dynamics, or to the low-fidelity riser model's wake oscillator implementation, requires further analysis and possibly the implementation of a different wake oscillator model for a more accurate comparison.

7

Future work

The purpose of this chapter is to suggest improvements to the models developed in this study and a wider application of the models to more complex simulation conditions.

7.1 Model improvements

7.1.1 OrcaFlex

In OrcaFlex, the riser model can be further improved by experimenting with other VIV prediction models. The Milan wake oscillator model or vortex tracking models may provide different dynamic riser response predictions under complex conditions, and such an analysis would be interesting to assess whether a lower vortex-induced vibrational response is tied to the global riser dynamics or rather the wake oscillator model type and setup.

7.1.2 Star-CCM+

In Star-CCM+, the accuracy of the fluid solver may be improved with finer mesh refinement, a lower solver time step, and adaptive mesh refinement, but they will significantly increase the computational time of the simulation. The structural coupling of the supports at the top and bottom ends of the segment can be investigated to better represent realistic structural behaviour. In addition, the equivalent density used to account for the inertia of the internal contents of the segment may be represented in a different manner, which would improve the accuracy of the solid stress solver, so that structural deformations are tied to the density of the steel only.

A deformable fluid body interaction model using overset mesh may alternatively be used to capture the VIV behaviour of the segment, in which the segment is treated as a rigid body. Since the segment is short, its high bending stiffness may make it suitable for rigid body motion. However, in this setup, the fluid-structure interaction does not include a solid stress solver, and therefore cannot be used for fatigue assessment by itself, unless it is coupled to an external FEM solver like Abaqus.

The FSI morpher setup used in this thesis is limited to relatively small mesh deformations. In instances of large structural motions, the DFBI with overset mesh may be particularly useful, since the overset mesh moves with the rigid body without stretching the surrounding mesh.

7.2 Extension of simulation conditions

Future work should consider the effects of a wider set of environmental conditions, including combined wave, wind, and current loads and extreme sea states. Long-term ocean statistics with wave scatter diagrams of the specified location, along with loop and tidal current velocity magnitudes, may be used to reproduce realistic local conditions of the sea state. The effect of the motion of the semi-submersible drilling platform should also be considered within this operating environment.

7.3 Model validation and experimental work

The model in this study was developed from model data used in a published research paper (Sevillano et al., 2013), but the final model is not the same as the originally referenced model due to the difference in riser operating conditions. Furthermore, the referenced research paper analyses fatigue metrics for a riser in the hang-off operating condition, which is not directly comparable to the results presented in this study. The results from the OrcaFlex model should then be validated against available field data. Future work should involve developing a riser model from an existing drilling riser, then validating the OrcaFlex model results with field data from the existing site. This is, however, challenging due to the lack of field data and riser configuration information from existing drilling risers. In Star-CCM+, experimental testing of a representational riser segment in a controlled environment should be used to validate VIV response results.

7.4 Application to full-scale riser systems

Future studies should investigate whether the methodology used in this study can be used reliably in realistic operating conditions, in which the riser experiences excitation loads at the surface. The modal behaviour of the riser may change, but if the methodology used to determine the riser segment's dynamic properties leads to similar response trends as in the current-only condition, then the methodology can be used reliably in other applications as well.

References

Bai, Y., & Jin, W.-L. (2016). Loads and dynamic response for offshore structures. In *Marine structural design* (pp. 119–151). Elsevier. https://doi.org/10.1016/b978-0-08-099997-5.00007-1

Cajas, J. C., Rodríguez, I., Salcedo, E., Lehmkuhl, O., Houzeaux, G., & Treviño, C. (2023). Aspect ratio influence on the vortex induced vibrations of a pivoted finite height cylinder at low Reynolds number. *Physics of Fluids*, *35*(8), 1–10. https://doi.org/10.1063/5.0164452

Carl M. Larsen. (2024, August). Marine dynamics course compendium. NTNU. https://www.ntnu.edu/studies/courses/TMR4182/2026#tab=omEmnet

Carvalho, I. A., & Assi, G. R. (2023). Passive control of vortex-shedding past finite cylinders under the effect of a free surface. *Physics of Fluids*, *35*(1), 11–13. https://doi.org/10.1063/5.0134730

Chen, H.-C., Chen, C.-R., & Mercier, R. S. (2006). CFD simulation of riser VIV, 13–18.

Griffin, O. M., Skop, R. A., & Koopmann, G. H. (1973). The vortex-excited resonant vibrations of circular cylinders. *Journal of Sound and Vibration*, *31*(2), 235–249. https://doi.org/10.1016/S0022-460X(73)80377-3

Gsell, S., Bourguet, R., & Braza, M. (2016). Two-degree-of-freedom vortex-induced vibrations of a circular cylinder at Re 3900. *Journal of Fluids and Structures*, *67*, 156–172. https://doi.org/10.1016/j.jfluidstructs.2016.09.004

Gustafsson, A. (2012). *Analysis of vortex-induced vibrations of risers* [Doctoral dissertation]. https://odr.chalmers.se/items/d8b184ea-7bb0-4c48-b73e-346622299756

Huang, W., Wu, X., Liu, J., & Bai, X. (2022). Dynamics of deepwater riser theory and method. https://doi.org/10.1007/978-981-16-2888-7

Jauvtis, N., & Williamson, C. H. (2003). Vortex-induced vibration of a cylinder with two degrees of freedom. *Journal of Fluids and Structures*, *17*(7), 1035–1042. https://doi.org/10.1016/S0889-9746(03)00051-3

Luo, S. C., Gan, T. L., & Chew, Y. T. (1996). Uniform flow past one (or two in tandem) finite length circular cylinder(s). *Journal of Wind Engineering and Industrial Aerodynamics*, *59*, 91–92. https://www.sciencedirect.com/science/article/abs/pii/0167610595000364

Matrix composites & engineering. (2026). Permanent buoyancy systems matrix composites & engineering. https://matrixengineered.com/wp-content/uploads/2024/03/matrix-permanent-buoyancy-solutions-brochure.pdf

Modarres-Sadeghi, Y. (2022, January). Introduction to fluid-structure interactions. In *Introduction to fluid-structure interactions* (pp. 1–83). Springer International Publishing. https://doi.org/10.1007/978-3-030-85884-1

Mottaghi, S., Gabbai, R., & Benaroya, H. (2020). Solid mechanics and its applications. http://www.springer.com/series/6557

NOAA. (2025). Ocean currents - National Oceanic and Atmospheric Administration. https://www.noaa.gov/education/resource-collections/ocean-coasts/ocean-currents

Orcina. (2025). OrcaFlex help. https://www.orcina.com/webhelp/OrcaFlex/

Orcina. (2026). B01 drilling riser. https://www.orcina.com/resources/examples/?key=b

Palfy, J. (2017). *Guidance notes on drilling riser analysis* (tech. rep.). https://ww2.eagle.org/content/dam/eagle/rules-and-guides/current/offshore/280_Guidance_Notes_on_Drilling_Riser_Analysis_2017/Drilling_Riser_Analysis_GN_e-July17.pdf

Poore, A. B., Doedel-
, E. J., & Cermak, J. E. (1986). Dynamics of the Iwan-Blevins wake oscillator model, 291–294. https://doi.org/10.1016/0020-7462(86)90036-3

Potts, D. A., Marcollo, H., & Jayasinghe, K. (2022). Strouhal number for vortex-induced vibration excitation of long slender structures. *Journal of Offshore Mechanics and Arctic Engineering*, *144*(4), 1–2. https://doi.org/10.1115/1.4054426

Sarpkaya, T. (1977). In-line and transverse forces on cylinders in oscillatory flow at high Reynolds numbers. *Journal of Ship Research*, *21*(4), 200–216. http://onepetro.org/JSR/article-pdf/21/04/200/2234786/sname-jsr-1977-21-4-200.pdf/1

Sevillano, L. C., Morooka, C. K., Ricardo, J., Mendes, P., & Miura, K. (2013). Drilling riser analysis during installation of a wellhead equipment, 1–3. https://doi.org/10.1115/OMAE2013-10554

Siemens. (2026). Simcenter STAR-CCM+ 2506 user guide. https://community.sw.siemens.com/s/question/0D54O000061xpUOSAY/simcenter-starccm-user-guide-tutorials-knowledge-base-and-tech-support

Williamson, C. H., & Jauvtis, N. (2004). A high-amplitude 2T mode of vortex-induced vibration for a light body in XY motion. *European Journal of Mechanics, B/Fluids*, *23*(1), 107–114. https://doi.org/10.1016/j.euromechflu.2003.09.008

Woo, N. S., Han, S. M., & Kim, Y. J. (2016). Design of a marine drilling riser for the deepwater environment. *Advances in Fluid Mechanics XI*, *1*, 233–242. https://doi.org/10.2495/afm160201

Xu, J. l., & Zhu, R. q. (2009). Numerical simulation of VIV for an elastic cylinder mounted on the spring supports with low mass-ratio. *Journal of Marine Science and Application*, *8*(3), 237–245. https://doi.org/10.1007/s11804-009-8117-x

Zhang, X., Zhang, X., Zhou, S., Yang, W., Xu, L., Yi, L., Tian, G., Ma, Y., Hao, Y., & Ni, W. (2023). A modified wake oscillator model for the cross-flow vortex-induced vibration of rigid cylinders with low mass and damping ratios.

Journal of Marine Science and Engineering, *11*(2), 1–5. https://doi.org/10.3390/jmse11020235

Zhao, M., & Cheng, L. (2014). Vortex-induced vibration of a circular cylinder of finite length. *Physics of Fluids*, *26*(1), 1–10. https://doi.org/10.1063/1.4862548

DEPARTMENT OF MECHANICS AND MARITIME SCIENCES
CHALMERS UNIVERSITY OF TECHNOLOGY
Gothenburg, Sweden
www.chalmers.se